Multi-Scale Spiking Network Model of Human Cerebral Cortex

Jari Pronold[1,2,†,*], **Alexander van Meegen**[1,3,†,*], **Hannah Vollenbröker**[1,4], **Renan O. Shimoura**[1], **Mario Senden**[5,6], **Claus C. Hilgetag**[7], **Rembrandt Bakker**[1,8], **Sacha J. van Albada**[1,3,*]

***For correspondence:**
a.van.meegen@fz-juelich.de (AvM);
j.pronold@fz-juelich.de (JP);
s.van.albada@fz-juelich.de (SvA)

[†]These authors contributed equally to this work

[1]Institute of Neuroscience and Medicine (INM-6) and Institute for Advanced Simulation (IAS-6) and JARA-Institute Brain Structure-Function Relationships (INM-10), Jülich Research Centre, 52428 Jülich, Germany; [2]RWTH Aachen University, 52062 Aachen, Germany; [3]Institute of Zoology, University of Cologne, 50674 Cologne, Germany; [4]Heinrich Heine University Düsseldorf, 40225 Düsseldorf, Germany; [5]Department of Cognitive Neuroscience, Faculty of Psychology and Neuroscience, Maastricht University, 6229 ER Maastricht, The Netherlands; [6]Maastricht Brain Imaging Centre, Faculty of Psychology and Neuroscience, Maastricht University, 6229 ER Maastricht, The Netherlands; [7]Institute of Computational Neuroscience, University Medical Center Eppendorf, Hamburg University, 20246 Hamburg, Germany; [8]Donders Institute for Brain, Cognition and Behavior, Radboud University Nijmegen, 6525 EN Nijmegen, The Netherlands

Abstract Although the structure of cortical networks provides the necessary substrate for their neuronal activity, the structure alone does not suffice to understand it. Leveraging the increasing availability of human data, we developed a multi-scale, spiking network model of human cortex to investigate the relationship between structure and dynamics. In this model, each area in one hemisphere of the Desikan-Killiany parcellation is represented by a $1\,\mathrm{mm}^2$ column with a layered structure. The model aggregates data across multiple modalities, including electron microscopy, electrophysiology, morphological reconstructions, and DTI, into a coherent framework. It predicts activity on all scales from single-neuron spiking activity to the area-level functional connectivity. We compared the model activity against human electrophysiological data and human resting-state fMRI data. This comparison reveals that the model can reproduce both spiking statistics and fMRI correlations if the cortico-cortical connections are sufficiently strong. Furthermore, we show that a single-spike perturbation propagates through the network within a time close to the limit imposed by the delays.

Introduction

Brain organization and activity display distinct features across multiple spatial and temporal scales: from the molecular level to whole-brain networks, from sub-millisecond processes to memories that last decades (***Deco et al., 2008***; ***Honey et al., 2012***; ***Squire et al., 2015***). Impressive technological advancements have made almost all these scales accessible through specialized techniques, which leads to a comprehensive but fragmented picture (***Sejnowski et al., 2014***). Models have the potential to integrate the diverse data modalities into a unified framework and to bridge across the scales (***Pulvermüller et al., 2021***).

Large-scale, data-driven models at cellular resolution have been constructed for sensory cortex

(*Reimann et al., 2013*; *Markram et al., 2015*; *Girardi-Schappo et al., 2016*; *Arkhipov et al., 2018*; *Billeh et al., 2020*), prefrontal cortex (*Hass et al., 2016*), hippocampus (*Hendrickson et al., 2012*; *Bezaire et al., 2016*; *Ecker et al., 2020*), cerebellum (*Casali et al., 2019*; *Yamaura et al., 2020*), and the olfactory bulb (*Migliore et al., 2014*, *2015*), among others. These models reproduce resting-state activity (e.g. *Potjans and Diesmann, 2014*; *Markram et al., 2015*; *Hass et al., 2016*; *Bezaire et al., 2016*) and stimulus responses (e.g. *Arkhipov et al., 2018*; *Billeh et al., 2020*) on various levels of detail. Advances in the simulation technology for large networks of point neurons (*Einevoll et al., 2019*; *Jordan et al., 2018*; *Pronold et al., 2022b*,a) have enabled the step beyond single brain regions to multi-area cortical network models (*Schmidt et al. 2018a*,b; see also *Izhikevich and Edelman 2008* for a pioneering study).

The multi-area spiking network model of *Schmidt et al.* (*2018b*) relates the connectivity of the vision-related areas in one hemisphere of macaque visual cortex to its dynamics. It integrates cortical architecture and connectivity data into a comprehensive, layer-resolved network of 32 areas. Axonal tracing data collected from the CoCoMac database (*Bakker et al., 2012*) and quantitative and layer-specific retrograde tracing experiments (*Markov et al., 2014b*,a) are used to establish the cortico-cortical connectivity. The connection probabilities derived by *Potjans and Diesmann* (*2014*) are used as a blueprint for local connectivity (*Schmidt et al., 2018a*). Simulations where the model is poised in a metastable regime just below a transition to a high-activity regime reproduce local and cortico-cortical experimental findings from resting-state activity (*Schmidt et al., 2018b*): single-cell spiking statistics, represented by firing rates and power spectra, closely match recordings in macaque V1, and functional connectivity patterns correspond well with macaque fMRI data. The model yields population bursts that mainly propagate in the feedback direction, akin to empirical findings during visual imagery (*Dentico et al., 2014*) and in slow-wave sleep (*Massimini et al., 2004*; *Nir et al., 2011*; *Sheroziya and Timofeev, 2014*).

Due to the scarcity of available data in comparison with other species, only a few large-scale cellularly resolved human brain network models have been built (*Izhikevich and Edelman, 2008*; *Lu et al., 2022*). The former encompasses a million neurons for most simulations (although a variant with 10^{11} neurons was also simulated), while the latter goes up to the full 86 billion neurons of human cortex. The model of *Izhikevich and Edelman* (*2008*) includes thalamocortical interactions and simulates self-sustained activity as well as chaotic cortical spiking activity (as observed experimentally by *London et al., 2010*; but see *Priesemann et al., 2014*). As it models each cortical area after early sensory cortex, it neglects the cytoarchitectural heterogeneity across areas. Likewise, the model of *Lu et al.* (*2022*) neglects heterogeneity for instance by using the same average number of incoming synapses per neuron in each brain area. Furthermore, both models do not focus on realistic laminar patterns of cortico-cortical connectivity, and considerably downscale the number of synapses per neuron. Such downscaling is likely to affect the obtained dynamics, such as the correlation structure of the activity (*van Albada et al., 2015*).

Leveraging the increasing availability of human data (e.g. *Mohan et al., 2015*; *Minxha et al., 2020*; *Cano-Astorga et al., 2021*; *Berg et al., 2021*; *Shapson-Coe et al., 2021*), we build and simulate a model that encompasses the scales from the single-neuron level to the network of areas in one hemisphere of the human brain. The model aggregates data across many scales, from electron microscopy data for the density of synapses (*DeFelipe et al., 2002*; *Cano-Astorga et al., 2021*) to whole-brain DTI and fMRI data, supplements it through predictive connectomics (e.g. *Barbas and Rempel-Clower, 1997*; *Ercsey-Ravasz et al., 2013*; *Beul et al., 2017*; *Hilgetag et al., 2019*; *van Albada et al., 2022*), and yields activity data on scales from single-neuron spiking activity to area-level correlation patterns.

Simulating large-scale models such as the multi-area model of macaque visual cortex or the model of human cortex presented here requires the efficient use of supercomputers, a thorough understanding of the inherent bottlenecks of these simulations, and state-of-the-art simulation technology. Systematic benchmarking is a significant step toward the optimal use of neuronal simulator technologies such as NEST (*Diesmann and Gewaltig, 2002*) on supercomputers (*van Al-*

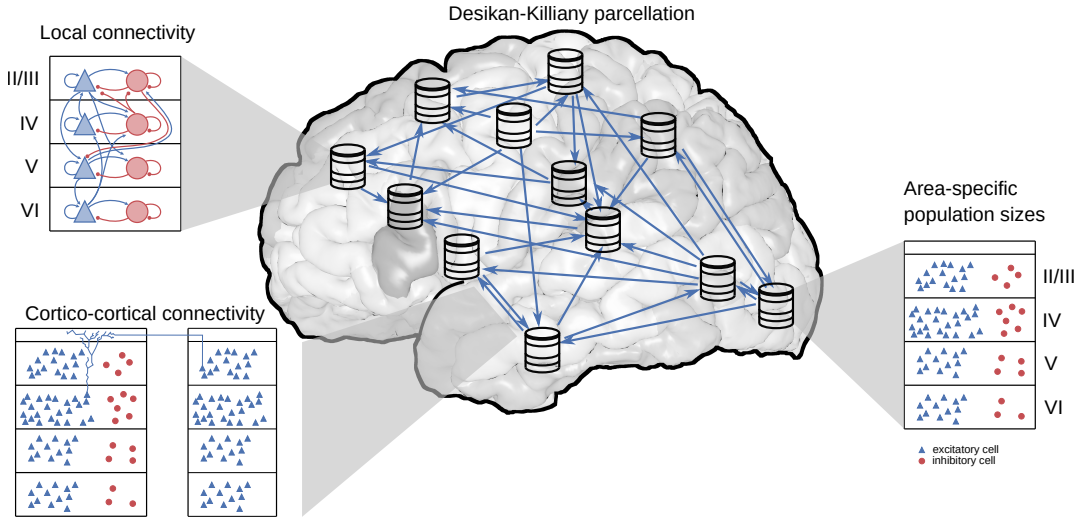

Figure 1. Model overview. The model comprises all 34 areas of the Desikan-Killiany parcellation (***Desikan et al., 2006***) in one hemisphere of human cerebral cortex. Each area is modeled by a column with $1\mathrm{mm}^2$ cortical surface. Within each column, the full number of neurons and synapses based on anatomical data is included. In total, this leads to 3.47 million neurons and 42.8 billion synapses. Both the intrinsic and the cortico-cortical connectivity are layer- and population-specific.

bada et al., 2021; ***Albers et al., 2022***). Furthermore, recent studies have systematically isolated and addressed major contributing factors to long simulation times (***Pronold et al., 2022b***,a). These optimizations, coupled with a relatively coarse brain parcellation, limit the simulation times for the model presented here. Shorter simulation times lead to a higher turnover rate of simulations, and enable investigations of more versions and realizations of a model.

First, we describe the data integration into a mesoscale connectome and its validation against features that were not explicitly built in. Then, we analyze the spiking activity in a version of the model with equal local and cortico-cortical synaptic strengths. We call this version with vanilla parameters the 'ground state' of the model (note that we do not use the term to refer to an energy minimum). The ground state lacks substantial cortico-cortical interactions, so we systematically increase the cortico-cortical synaptic weights. Next, we compare the resulting activity with single-neuron spiking statistics and area-level correlation patterns based on fMRI. The experimental data is reproduced best when cortico-cortical synaptic weights are increased relative to local synaptic weights. We refer to the state of the model with the smallest cortico-cortical weight scaling factor for which the experimental data are well reproduced as the 'best-fit state'. Finally, we investigate how a single-spike perturbation propagates through the network and find rapid spike propagation in both ground state and best-fit state.

Results

Human Mesoscale Connectome

The model comprises all 34 areas of one hemisphere of human cortex in the Desikan-Killiany parcellation (***Desikan et al., 2006***). Each area is modeled by a $1\ \mathrm{mm}^2$ column and the columns are connected through long-range projections (see Fig. 1). We here give an overview of the model construction. A more detailed derivation can be found in Sec. Materials & Methods.

We distinguish two classes of neurons, excitatory and inhibitory, and account for the layered structure of cortex. We determine the number of neurons from their volume density, the layer thickness, and the surface area of the column (***Von Economo, 2009***; cf. Sec. Neuron number). The parameters of the neurons are derived from the Allen Cell Types Database (https://celltypes.brain-map.org/; cf. Sec. Further Parameters of the Model). At this level of modeling, the connec-

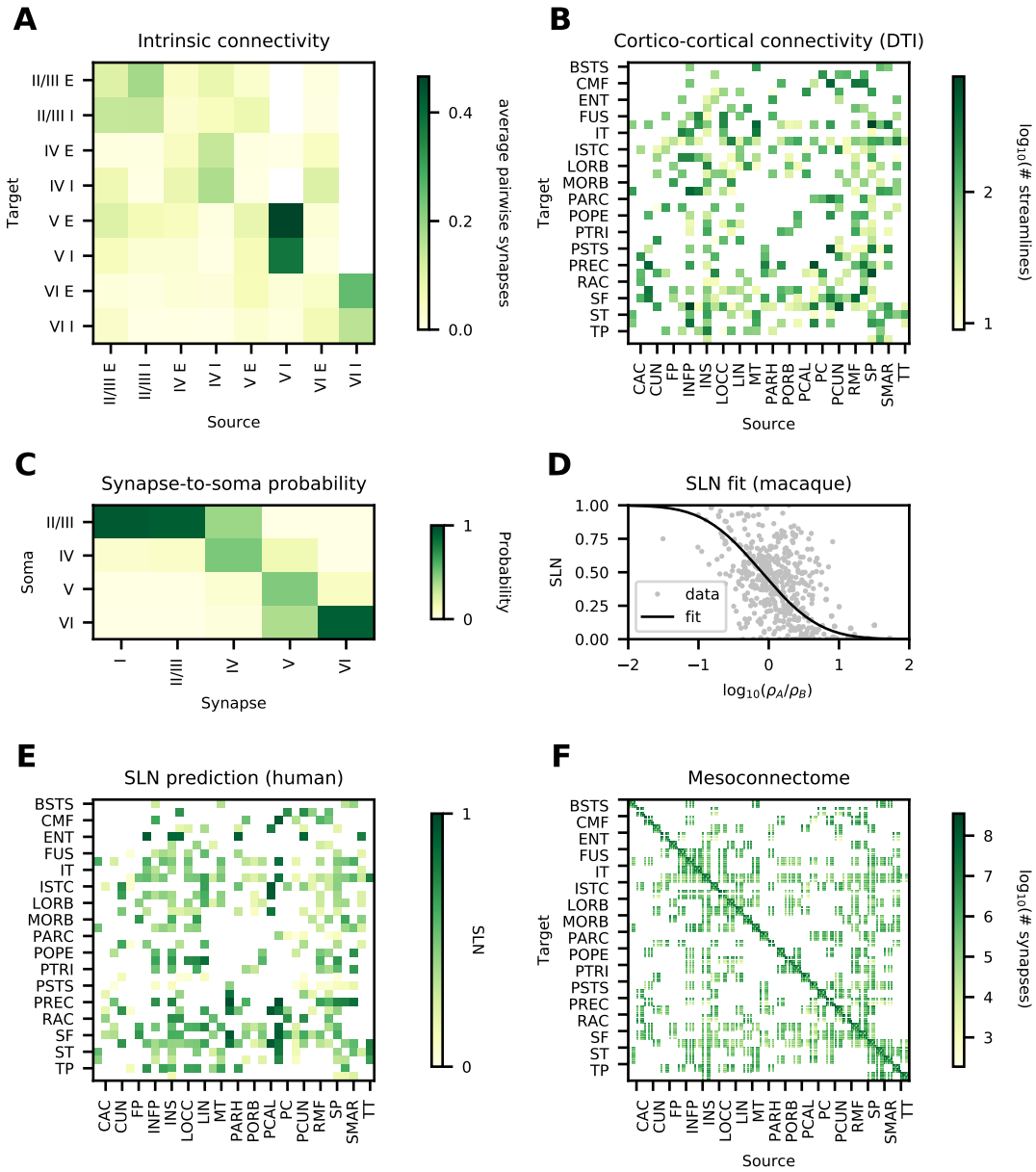

Figure 2. Data and predictive connectomics. (**A**) Within-area connectivity blueprint (average number of synapses per pair of neurons). (**B**) Cortico-cortical connectivity based on DTI (number of streamlines); see Table 1 for acronyms. (**C**) Probability for cortico-cortical synapses in a given layer to be established on neurons with cell body in a given layer, estimated from human neuron morphologies. (**D**) Relation of neuron densities of source area *B* and target area *A* with laminar source pattern (fraction of supragranular labeled neurons, SLN) in macaque. (**E**) Predicted source pattern (SLN) in human. (**F**) Layer- and population-resolved mesoconnectome (number of synapses).

Long name	Acronym	Long name	Acronym
bankssts	BSTS	parsorbitalis	PORB
caudalanteriorcingulate	CAC	parstriangularis	PTRI
caudalmiddlefrontal	CMF	pericalcarine	PCAL
cuneus	CUN	postcentral	PSTS
entorhinal	ENT	posteriorcingulate	PC
fusiform	FUS	precentral	PREC
inferiorparietal	INFP	precuneus	PCUN
inferiortemporal	IT	rostralanteriorcingulate	RAC
isthmuscingulate	ISTC	rostralmiddlefrontal	RMF
lateraloccipital	LOCC	superiorfrontal	SF
lateralorbitofrontal	LORB	superiorparietal	SP
lingual	LIN	superiortemporal	ST
medialorbitofrontal	MORB	supramarginal	SMAR
middletemporal	MT	frontalpole	FP
parahippocampal	PARH	temporalpole	TP
paracentral	PARC	transversetemporal	TT
parsopercularis	POPE	insula	INS

Table 1. All 34 areas in the Desikan-Killiany parcellation for one hemisphere with corresponding acronyms.

tivity statistics between neurons in both classes and all layers are needed, which are not straightforwardly delivered by current experimental techniques. Accordingly, we combine available data with predictive connectomics to arrive at a human mesoconnectome at a layer- and population-resolved level.

The lack of data on the connectivity is the main reason for considering only two classes of neurons. While a recent study defines 45 inhibitory and 24 excitatory neuron types in human (***Hodge et al., 2019***), including this diversity would require a huge number of cell-type-specific connection probabilities. This is not yet feasible because no connectivity data is available at such a fine granularity; hence, we restrict the model to two classes of neurons, as done in earlier studies (***Potjans and Diesmann, 2014***; ***Schmidt et al., 2018a***,b).

To derive the mesoconnectome, we start from a synapse-centric perspective. We approximate the volume density of synapses $\rho_{\text{synapse}} = 6.6 \times 10^8\ \text{synapses/mm}^3$ (***Cano-Astorga et al., 2021***) as constant across cortex (***DeFelipe et al., 2002***; ***Sherwood et al., 2020***), which allows us to compute the total number of synapses per layer based on their respective thickness (***Von Economo, 2009***). The task that remains is to determine the pre- and post-synaptic neurons of these synapses.

Data Aggregation and Predictive Connectomics

In a first step, we separate the synapses into local (within-area) connections and long-range projections by extrapolating the value of 79% local connections based on tracing data in macaque (***Markov et al., 2011***) to 86% in human using the power-law relation between local connections and total number of neurons (***Herculano-Houzel et al., 2010***; cf. Sec. Fraction of Cortico-Cortical Connections). For the local connections, we use the connection probabilities derived by ***Potjans and Diesmann*** (***2014***) (Fig. 2**A** and Local Connectivity) as a blueprint. The relative connection probabilities across source and target populations are kept constant, and they are only scaled by a constant factor to achieve the desired total number of local synapses in each area. The cortico-cortical connectivity on the area level is specified by DTI data from the Human Connectome Project (***Goulas et al., 2016***, which is based on the data from ***Van Essen et al., 2013***; Fig. 2**B** and Long-range projections). Synapses associated with long-range projections are assigned to postsynaptic neurons according to morphological reconstructions of human neurons (***Mohan et al., 2015***; Fig. 2**C** and Long-range projections).

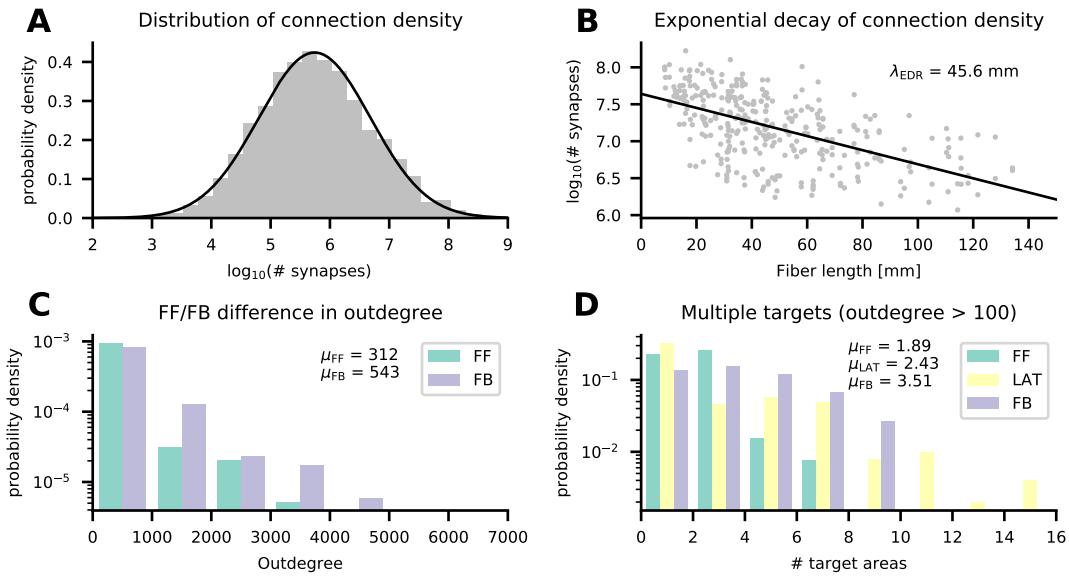

Figure 3. Connectivity validation. (**A**) Histogram of the number of synapses between pairs of populations (gray bars) and a log-normal fit (black line). (**B**) Logarithmic number of synapses between a pair of areas versus distance between these areas (gray symbols) and an exponential fit (black line). (**C**) Average outdegree of a neuron in any given population to any postsynaptic area in either feedforward (FF) or feedback (FB) direction. (**D**) Average number of target areas of a neuron in any given population to any postsynaptic area with average outdegree larger than 100 in either feedforward (FF), lateral (LAT), or feedback (FB) direction.

The laminar origin of long-range projections is based on predictive connectomics. Retrograde tracing data in macaque shows that the laminar origin is systematically related to the cytoarchitecture (***Hilgetag et al., 2019***; Fig. 2**D**). Assuming that the same relation also holds in human, we use the fit in combination with the human cytoarchitecture to determine the laminar origin (Fig. 2**E**). For the laminar target, we assume the same relation between laminar origin and target as done for macaque by ***Schmidt et al.*** (***2018a***), for lack of layer-specific human data.

Combining this data, we arrive at a human mesoconnectome which specifies the number of synapses between excitatory and inhibitory neurons for all areas in the Desikan-Killiany parcellation on a layer- and population-specific level (Fig. 2**F**).

Connectivity Validation

To validate the derived mesoconnectome, we compare it with anatomical features which were observed in other species but which were not explicitly built in.

The density of connections between areas is highly heterogeneous, spanning five orders of magnitude, and approximately log-normally distributed in mouse (***Gămănuţ et al., 2018***), marmoset (***Theodoni et al., 2021***), and macaque (***Ercsey-Ravasz et al., 2013***). Similarly, in our model the numbers of synapses between pairs of populations span five orders of magnitude (Fig. 3**A**) and they are approximately log-normally distributed. Furthermore, the connection density decays exponentially with distance in mouse (***Horvát et al., 2016***), marmoset (***Theodoni et al., 2021***), and macaque (***Ercsey-Ravasz et al., 2013***). In our model, the number of synapses between pairs of areas also decays exponentially (Fig. 3**B**) with a decay constant of $45.6\,\mathrm{mm}$. Thus, two salient features of tracing data are captured by our model.

Anterograde tracing data indicate that feedback axons arborize more strongly than their feedforward counterparts (***Rockland, 2019***). This suggests a larger outdegree of feedback projections compared to feedforward projections. In our model, the average outdegree from neurons in a given population to a given target area varies systematically between feedforward and feedback projections (Fig. 3**C**); here, feedforward and feedback were classified based on the predicted SLN

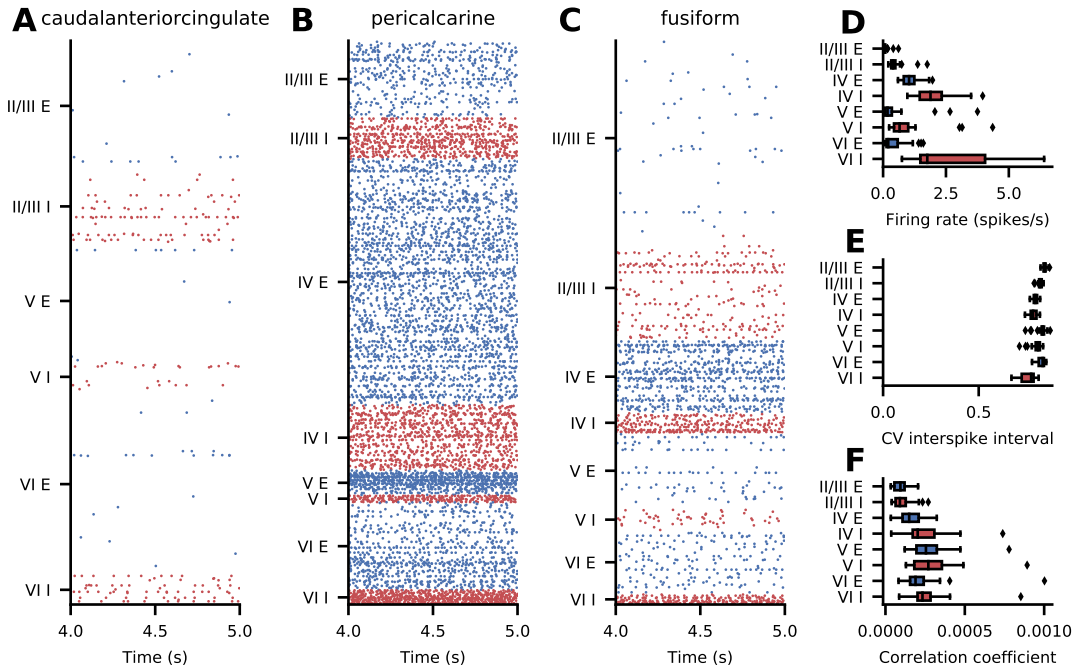

Figure 4. Ground-state spiking activity of the model. (**A**-**C**) Raster plots for three representative areas; subsampled to 2.5% of the excitatory (blue) and inhibitory (red) neurons. (**D**-**F**) Layer- and population-resolved distribution of population-averaged statistics across areas; boxes show quartiles, whiskers are within 1.5 times the interquartile range, symbols show outliers outside of the whiskers. (**D**) Firing rate. (**E**) Coefficient of variation of the interspike intervals of neurons with at least 10 spikes. (**F**) Correlation coefficient of a random subsample of 2000 neurons for each population.

value (***Schmidt et al., 2018a***): $\mathrm{SLN} > 65\%$ (feedforward), $35\% \leq \mathrm{SLN} \leq 65\%$ (lateral), and $\mathrm{SLN} < 35\%$ (feedback). The average outdegree for feedforward inter-area connections in our model is 312 compared to 543 in the feedback direction.

Finally, fully reconstructed axons (***Winnubst et al., 2019***) suggest that many projecting neurons target multiple areas. To check for such divergence in the model, we restrict ourselves to connections with an average outdegree larger than 100. Again using the predicted SLN value to separate feedforward, lateral, and feedback connections, we obtain a broad distribution of the number of target areas (Fig. 3**D**). In addition to the larger outdegree in the feedback direction, feedback projections also target more areas: on average 3.51 compared to 2.43 for lateral and 1.89 for feedforward projections.

Micro- and Macroscopic Dynamics

Ground-state Spiking Activity

The simulated spiking activity of the ground-state version of the model is asynchronous and irregular with low firing rates across all areas (Fig. 4). There is a pronounced structure of the activity across populations, layers, and areas (Fig. 4**A**-**C**).To quantify the spiking activity further, we consider population-averaged statistics (Fig. 4**D**-**F**). The firing rate of the inhibitory neurons is higher than the firing rate of the excitatory neurons, with the highest activity in layer VI (Fig. 4**D**). The activity of some excitatory populations is very low, in particular in layers II/III and V (Fig. 4**D**). In terms of the irregularity of the spike trains, quantified by the coefficient of variation CV of the interspike interval, all populations are in the regime of $\mathrm{CV\ ISI} \approx 0.8$ (Fig. 4**E**), i.e., slightly more regular than a Poisson process. Lastly, the average pairwise correlation between the neurons is close to zero across all populations (Fig. 4**F**).

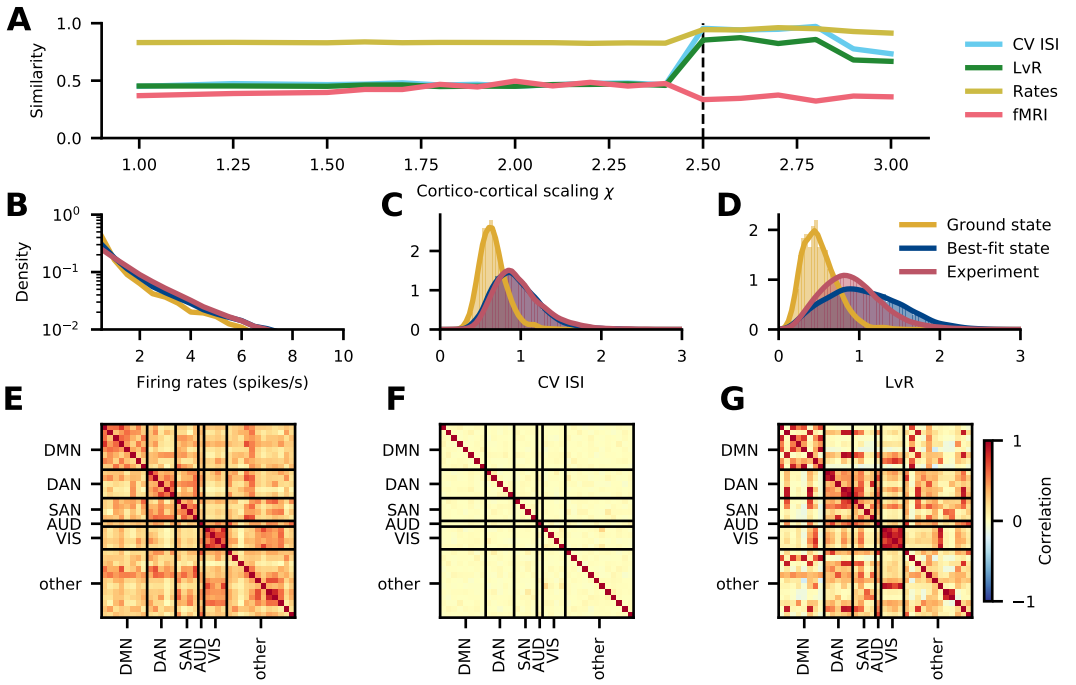

Figure 5. Comparison with experimental activity data. (**A**) Similarity of simulated spiking activity in area caudalanteriorcingulate to experimental spiking data (***Minxha et al., 2020***) recorded in medial frontal cortex and to resting-state fMRI functional connectivity (cf Sec. fMRI data) as a function of the scaling parameter χ for cortico-cortical synaptic strengths. The vertical dashed line at 2.5 corresponds to the chosen best-fit state. (**B-D**) Distribution of spiking statistics across neurons in experimental spiking data (***Minxha et al., 2020***) and in the simulated ground and best-fit states: Distribution of firing rates (**B**), coefficients of variation of the interspike interval (CV ISI) (**C**), and revised local variation (LvR; ***Shinomoto et al., 2009***) (**D**). (**E-G**) Functional connectivity in the default mode network (DMN), dorsal attention network (DAN), salience network (SAN), auditory network (AUD), visual network (VIS), and the remaining areas (other). Experimental functional connectivity of the right hemisphere from fMRI recordings averaged across nineteen subjects (**E**). Simulated functional connectivity based on synaptic input currents in the ground (**F**) and best-fit state (**G**).

Comparison With Experimental Activity Data

To obtain stronger inter-areal interactions, we increase the cortico-cortical synaptic weights onto excitatory neurons by the cortico-cortical scaling factor χ and onto inhibitory neurons by a factor $\chi_I \chi$, where $\chi_I = 2$. We compare the resulting activity of the model with experimental activity data on two levels: on the neuron level, we use the electrophysiological recordings by ***Minxha et al.*** (***2020***) from human medial frontal cortex (cf. Sec. Spiking data); on the cortex level, we use resting-state fMRI data from nineteen subjects (cf. Sec. fMRI data).

The electrophysiological data were recorded in dorsal anterior cingulate cortex as well as pre-supplementary motor area; we compare the data with the model activity in area caudalanteriorcingulate). Since the recordings are not layer- or population-specific, we combine the spike trains of all layers and populations in caudalanteriorcingulate for this analysis. In both the experimental and simulated data, we consider only neurons with at least 0.5 spikes/s for the firing rate, and, for the irregularity, expressed as the coefficient of variation of the interspike interval (CV) and revised local variation (LvR ***Shinomoto et al., 2009***), we consider only neurons with at least 10 spikes in the respective interval. As the spike trains comprise only two seconds of activity, we divide the ten seconds of simulated activity into five snippets of equal length. In order to compare the experimental and simulated distributions, we calculate the Kolmogorov-Smirnov distances between them and report $1 - KS_{dist}$ as a measure of similarity, where 0 means no and 1 means perfect similarity. To obtain a proxy for the BOLD signal from our model, we use the absolute value of the area-level

synaptic currents (***Schmidt et al., 2018b***). We compute the functional connectivity using the Pearson correlation coefficient of this BOLD proxy (simulation) or the BOLD signal (experiment). As a measure of the similarity between the modeled and empirical functional connectivity we also use the Pearson correlation coefficient, excluding the diagonal where all values are identically one.

Fig. 5**A** shows how the different similarity measures depend on the cortico-cortical scaling factor χ. The agreements of the $\mathrm{CV\ ISI}$, the LvR, and the rates initially stay constant and these measures abruptly show a higher agreement at $\chi = 2.5$. At χ values around the best-fit state, the network might start in a state of high activity and then, after an initial transient, settle in a lower-activity state or, depending on the random seed, the network might operate in a higher- or lower-activity state for the same value of χ altogether. To exclude transients due to a transition from a high- to low-activity state, we disregard the first $2500\,\mathrm{ms}$.The distributions of the spiking activity measures continue to match the experimental data well until $\chi = 2.8$. Afterwards, the similarities of the irregularity measures $\mathrm{CV\ ISI}$ and LvR deteriorate. The similarity of the fMRI functional connectivity grows from 0.37 to 0.47 and then suddenly drops to 0.33 at $\chi = 2.5$, a value around which it remains. The correlation of all experimental functional connectivities is 0.63. As $\chi = 2.5$ is the first point at which most measures show good agreement, we use this setting for further analysis. In the following, we refer to this setting as 'the best-fit state'.

A closer look at the underlying statistics (Fig. 5**B-D**) confirms that the best-fit state matches the experimental data better than the ground state does. The firing rate distribution (Fig. 5**B**) is reproduced well by both the ground and the best-fit state, but the latter follows the experimental distribution slightly better. This matches the observation in Fig. 5**A,** where the firing rate similarity is high throughout and peaks at the best-fit state. The $\mathrm{CV\ ISI}$ (Fig. 5**C**) shows clear differences between the ground and best-fit state: in the former, the $\mathrm{CV\ ISI}$ is narrowly distributed around a sub-Poissonian average; in the best-fit state and the recordings, the $\mathrm{CV\ ISI}$ is broadly distributed around a Poissonian average. These two distributions match almost exactly. Similar observations hold true for the LvR, where the main difference compared to the $\mathrm{CV\ ISI}$ is that all distributions are slightly broader.

To facilitate the comparison of the functional connectivities, we group the areas into clusters of different resting-state networks following ***Kabbara et al.*** (***2017***). The experimental (Fig. 5**E**) and best-fit (Fig. 5**G**) functional connectivities show a clear structure with increased correlations within the clusters in the resting state networks, while the functional connectivity of the ground state shows only very weak correlation (Fig. 5**F**). Also the enhanced correlations between the dorsal attention network (DAN) and the salience network (SAN) are well captured by the model in the best-fit state.

Analysis of Best-Fit State

The simulated spiking activity in the best-fit state varies across areas both quantitatively and qualitatively. Generally, firing rates are higher in the best-fit state than in the ground state (Fig. 6). Some areas, such as caudalanteriorcingulate (Fig. 6**A**) and fusiform (Fig. 6**C**), show low-rate uncorrelated spiking activity with brief population bursts, while some areas, such as pericalcarine, are in a state of high firing in most populations. For completeness, the raster plots of all areas are shown in Fig. 13, 14, 15. We consider population-averaged statistics to quantify the spiking activity on the level of the full network (Fig. 6**D**-**F**). Inhibitory neurons have higher firing rates than excitatory neurons, with the highest activities in layers IV and VI (Fig. 6**D**). The activity of some excitatory populations is very low, particularly in layers II/III, IV, and VI. The irregularity of the spike trains, quantified by the coefficient of variation of the interspike intervals ($\mathrm{CV\ ISI}$), is on average closer to that of a Poisson process compared to the ground state, but also varies more strongly across areas (Fig. 6**E**). The average pairwise correlations are generally low, but reach higher values in a number of areas (Fig. 6**F**).

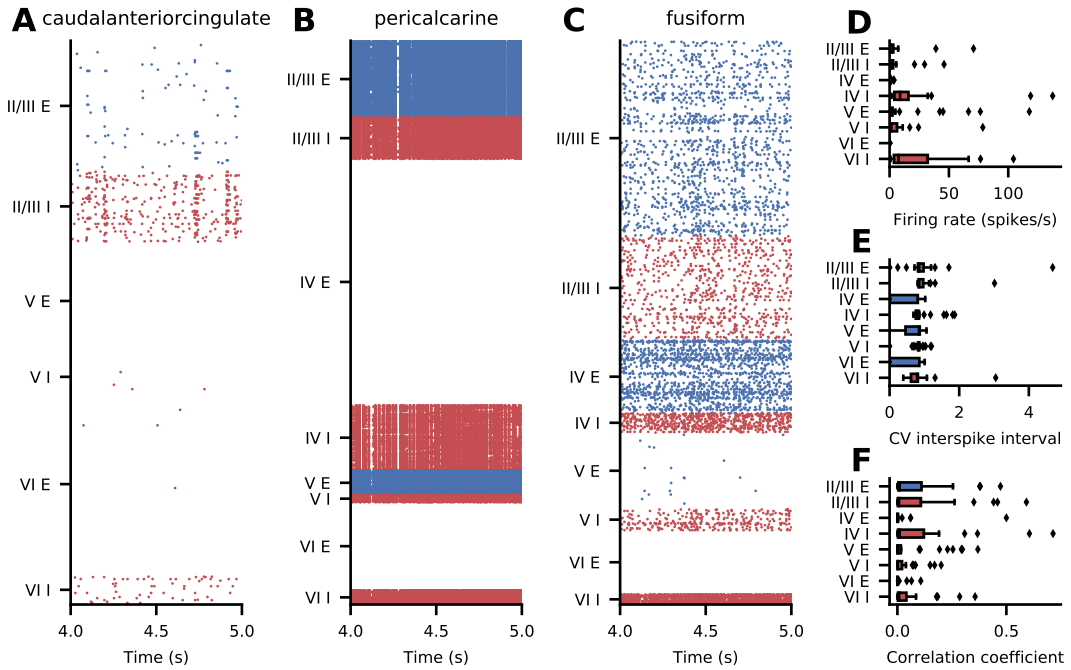

Figure 6. Best-fit spiking activity of the model. (**A**-**C**) Raster plots for three representative areas; subsampled to 2.5% of the excitatory (blue) and inhibitory (red) neurons. (**D**-**F**) Layer- and population-resolved distribution of population-averaged statistics across areas; boxes show quartiles, whiskers are within 1.5 times the interquartile range, symbols show outliers outside of the whiskers. (**D**) Firing rate. (**E**) Coefficient of variation of the interspike intervals (CV ISI) of neurons with at least 10 spikes. (**F**) Correlation coefficient of a random subsample of 2000 neurons for each population.

Propagation of a Single-Spike Perturbation

In vivo, single-neuron perturbations can affect behavior (***Brecht et al., 2004***; ***Houweling and Brecht, 2008***). But how does a single-neuron perturbation spread across the cortical network consisting of millions of neurons or more? We investigate this in our model comprising 3.5 million neurons. To this end, we perturb the membrane potential of a single excitatory neuron in layer IV in primary visual cortex (area pericalcarine) such that it exceeds the threshold and emits a spike. On the network level, this is an extremely weak perturbation. However, since spiking networks are highly sensitive to perturbations (***London et al., 2010***; ***Monteforte and Wolf, 2010***), even a single spike can alter the spiking pattern of the network (***Izhikevich and Edelman, 2008***).

We perform two simulations with identical parameters and random seeds but once without and once with the single-neuron perturbation. The drawn random numbers and their total number are the same in both simulations. To quantify alterations of the spiking pattern, we count the total number of spikes of a population in $0.1\,\mathrm{ms}$ bins and compute the difference between the unperturbed and the perturbed simulation. As soon as the difference is nonzero due to an additional or missing spike, our observable is set to one. Thus, the observable quantifies the presence or absence of a spike in a given population due to the perturbation. In both the ground state (Fig. 7**A**) and the best-fit state (Fig. 7**B**), the perturbation propagates to all areas in less than $50\,\mathrm{ms}$. In the best-fit state, the perturbation propagates even slighly faster to most areas (Fig. 7**C**). Presumably, the increased number of spikes in the best-fit state contributes to this difference in propagation speed (Fig. 6). In the ground state, the mean propagation time is $29.4\,\mathrm{ms}$ with a standard deviation of $10.9\,\mathrm{ms}$; in the best-fit state, the mean propagation time is $25.1\,\mathrm{ms}$ with a standard deviation of $10.4\,\mathrm{ms}$.

How is this fast propagation possible? Just like weighted area-level cortical graphs of mice and macaques (***Bassett and Bullmore, 2017***), the population-level graph in our model exhibits small-

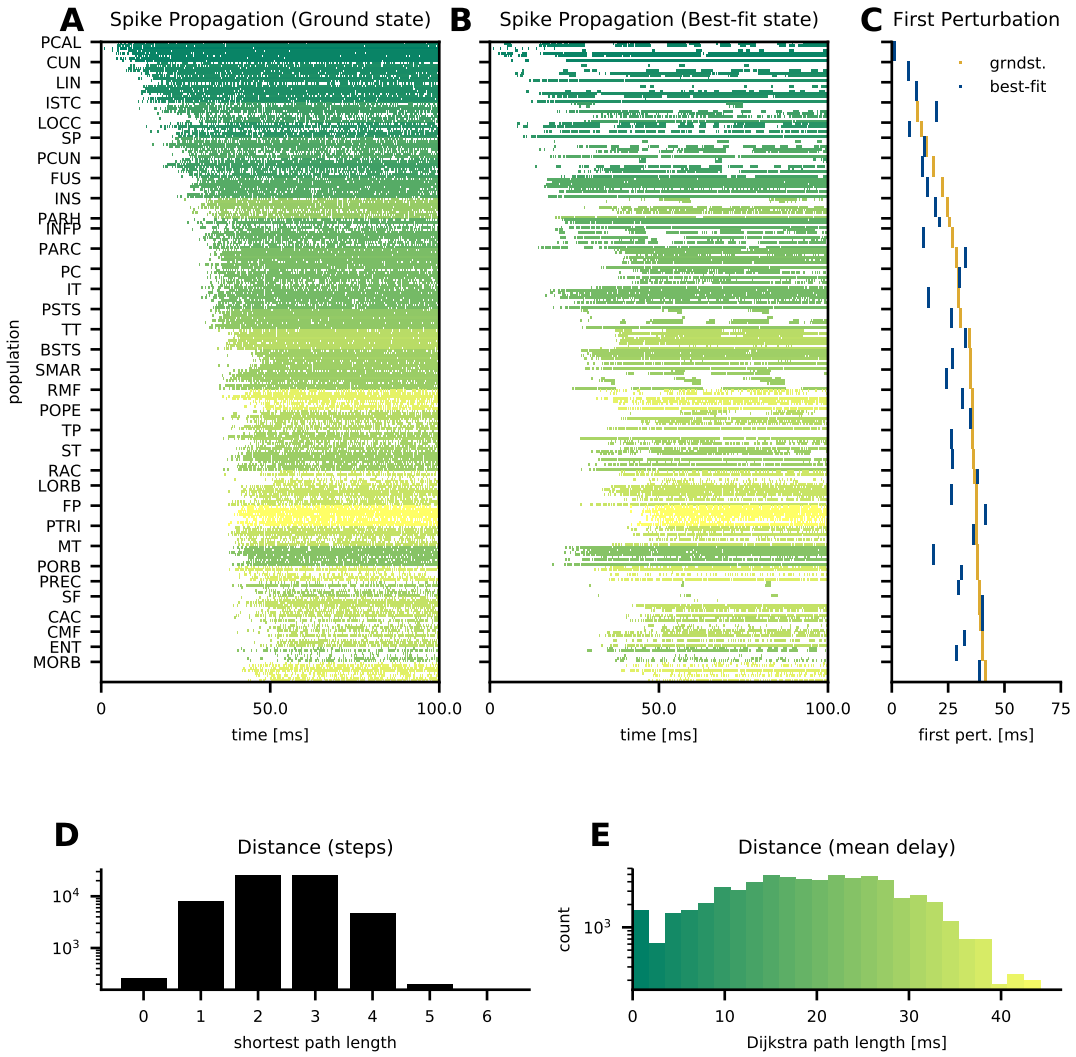

Figure 7. Propagation of a single spike. Binary absolute difference of spike counts in $0.1\,\mathrm{ms}$ bins between a perturbed and an unperturbed simulation with identical parameters and random seeds in the ground state (**A**) and the best-fit state (**B**); the color quantifies the Dijkstra path length between the perturbed and the target population. For the scale, see panel E. Timing of the first spike count difference per area (**C**) in the ground state (yellow) and the best-fit state (blue). Histogram of shortest path lengths between all pairs of populations in the network (**D**). Histogram of shortest path lengths weighted by the average delay between all pairs of populations in the network (**E**).

world network properties (***Watts and Strogatz, 1998***). Namely, only a small number of steps is needed to reach any node: the shortest path length between any pair of populations is between one and four and at most five (Fig. 7**D**). But the shortest path length in terms of the number of populations traversed does not account for the transmission delay, which is particularly relevant between areas. Taking also the delay into account by weighting each step with the mean delay and computing the Dijkstra path length (***Dijkstra, 1959***), i.e., the shortest path based on the sum of the delays, we see that the small-world property of the network enables a Dijkstra path length below $50\,\mathrm{ms}$ for any pair of populations and below $40\,\mathrm{ms}$ for the majority of pairs (Fig. 7**E**). Thus, the network structure supports fast propagation at the population level. The propagation of the perturbation indeed takes place on a timescale similar to the Dijkstra path length between the perturbed population and the target population. The distribution of delays (present in both model versions) in principle allows propagation to take place even faster than this path length.

Discussion

We aggregated data across multiple modalities, including electron microscopy, electrophysiology, morphological neuron reconstructions, and diffusion tensor imaging (DTI), to construct a multi-scale spiking network model of human cortex. In this computational model featuring 3.5 million neurons connected via 43 billion synapses, each area in a full hemisphere of human cortex is represented by a millimeter-scale layer-resolved microcircuit with the full density of neurons and synapses. The model was simulated on a supercomputer, making use of advances in the simulation technology of NEST. We filled gaps in the data using statistical regularities found in other species, in particular to determine the laminar origins and targets of cortico-cortical connections. Comparisons with electrophysiological recordings from human medial frontal cortex and human fMRI reveal that the model captures both microscopic and macroscopic resting-state activity when the strength of the cortico-cortical synapses is increased.

Simulations of the model with equal local and cortico-cortical synaptic strengths reveal a state with asynchronous and irregular activity, which we refer to as the 'ground state' of the model. The activity is heterogeneous across areas, layers, and excitatory and inhibitory populations. The ground-state activity deviates from the experimental recordings in terms of both spiking activity and inter-area functional connectivity. On the single-neuron level, the distribution of the spiking irregularity in the model is more narrow than the observed one and centered in the sub-Poissonian regime. On the network level, the activity is hardly correlated between areas, which is in stark contrast to the salient structure in the fMRI data.

To alleviate these discrepancies, we increased the synaptic weights of cortico-cortical connections. The increased anatomical connection strength leads to an increase in inter-areal correlations, with a modular structure similar to the experimental data. On the level of the single-neuron statistics, the increased cortico-cortical synaptic weights hardly affect the distribution of firing rates and irregularity until the synaptic weights reach a critical value at which the fit to the experimental data suddenly improves. This best-fit state features not only stronger correlations between the activity in different areas but also within areas and populations. Furthermore, the firing rates, in particular in the inhibitory populations, are increased. Although the low overall firing rates and the higher inhibitory compared to excitatory rates are realistic features, some layers and populations of the model exhibit either excessive or nearly vanishing rates. This uneven distribution of spiking activity across layers and populations remains to be addressed in future.

Computational models allow one to address questions that are hard to investigate experimentally. Here, we use our model to track the effect of a single additional spike through the large-scale network. We find that the single-spike perturbation spreads across the entire network within less than $50\,\mathrm{ms}$, close to the lower limit imposed by the mean transmission delay between the areas along the shortest possible path. In the best-fit state the propagation is even faster than in the ground state. The observed latencies are on the same order as visual response latencies across macaque cortex (***Lamme and Roelfsema, 2000***), but note that single-spike perturbations

may not be visible on the population level. Rapid propagation of spiking activity, whether on the single-neuron or the population level, is likely to support fast sensory processing and behavioral responses.

The approach we followed closely resembles that taken for the multi-area model of macaque vision-related cortex of ***Schmidt et al.*** (***2018a***,b). A notable difference compared to that model is that our best-fit state is stable over the full length of the investigated simulations, in contrast to the metastable activity obtained there. In the best-fit state, our model still exhibits a type of metastability: in some simulations, the activity is initially low and later switches to the higher-activity state that matches the experimental data better and that we analyze. This situation was reversed in the macaque model, where the best-fit state could switch at some point to a state with network-wide excessive activity. The increased stability of the best-fit state in the present model and the lack of excessive network-averaged firing rates throughout the simulations provide a better match to actual brain activity.

Just like the model of ***Schmidt et al.*** (***2018a***,b), the present model predicts that stronger cortico-cortical compared to local synapses are needed to account for appreciable functional connectivity between areas, a feature that may be investigated in future experiments. In our model, the cortico-cortical synapses are, moreover, stronger onto inhibitory than onto excitatory neurons. However, using older estimates of the relative densities of excitatory and inhibitory neurons (***Binzegger et al., 2004***; ***Potjans and Diesmann, 2014***), we were also able to obtain good correspondence with experimental resting-state activity in simulations with very strong cortico-cortical synapses, equal in strength onto excitatory and inhibitory neurons (Fig. 12). In this case, stability was afforded by stronger local synapses onto inhibitory compared to excitatory cells, consistent with recent slice data from human cortex (***Campagnola et al., 2022***). In all cases, we did not need to adjust the connection densities to obtain plausible activity as done in the macaque model (***Schuecker et al., 2017***). This is an improvement because now the connection densities can be directly estimated from the empirical data.

Various assumptions and approximations flow into the model definition. For instance, with the modeled inhibitory postsynaptic potentials being five times as large as excitatory ones, the relative strength of inhibitory synapses is rather high in the model, in-vitro recordings suggesting a factor closer to 1 (***Campagnola et al., 2022***). However, reducing the IPSP-to-EPSP ratio even to a value of 2 does not allow adequate reproduction of the observed microscopic and macroscopic activity statistics (see Fig. 9). In addition, the electrophysiological properties of individual neurons are known to be distributed, as characterized in detail in the Allen Cell Types Database (***Teeter et al., 2018***). However, using distributions based on the human neuron parameters provided by the Allen Cell Types Database leads to a worse fit to the experimental data compared to using the mean values only (see Fig. 10). A possible reason is that, in reality, intrinsic neuron parameters and input strengths are attuned to each other, preventing neurons with high intrinsic excitability from being strongly driven (***Joseph and Turrigiano, 2017***). Another example is that we assumed the fraction of cortico-cortical connections to equal the fraction of white-matter connections; however, cortical areas, especially adjacent ones, may also be connected to some extent via the gray matter (***Vandevelde et al., 1996***; ***Anderson and Martin, 2009***). Furthermore, the synaptic time constants for excitatory and inhibitory connections are taken to be equal in the model, whereas these have been found to differ in nature (***Spruston et al., 1995***; ***Salin and Prince, 1996***; ***Angulo et al., 1999***; ***Gupta et al., 2000***). Using longer inhibitory than excitatory time constants does not yield a state where the firing rate and irregularity distributions are simultaneously well reproduced in the present model (see Fig. 11). Further research may show how the model can be made consistent with these various biological features.

Besides qualitative approximations made in the model, detailed parameter values may also be updated in future, as additional data for human cortex are becoming available. For instance, layer- and cell-type-specific connection probabilities, synaptic strengths, and parameters of synaptic dynamics were recently measured in acute slices of human frontotemporal cortex (***Campagnola et al.,***

2022). Furthermore, the recent electron microscopic reconstruction of a millimeter-scale fragment of human temporal cortex (***Shapson-Coe et al., 2021***) delivers layer- and cell-type-specific local connectivity data that may be used to adjust the microcircuit connectivity used here. A new freely available dataset aligns block face images and microscopic sections stained for histology or immuhistochemistry with 7-T MRI images for two human brains (***Alkemade et al., 2022***). Furthermore, detailed human cytoarchitecture and receptor densities are gathered in the BigBrain (***Amunts et al., 2013***; ***Wagstyl et al., 2020***; ***Zachlod et al., 2023***), and are still being complemented with new measurements. These data follow the Julich-Brain parcellation (***Amunts et al., 2020***), which is more fine-grained than the Desikan-Killiany parcellation used here. Thus, the data may be leveraged either by finding an appropriate mapping between parcellations or by increasing the granularity of the model.

Experimental functional connectivity is not stationary but exhibits slow fluctuations (***Deco et al., 2011***). Currently, our model does not exhibit dynamics on such long timescales; we hypothesize that additional slow processes like spike-frequency adaptation, short-term plasticity, or neuromodulation are necessary to this end. Our model provides a starting point for investigating such processes via simulation. More generally, it enables in silico studies of the multi-scale dynamics of the human cerebral cortex and the information processing it supports, from the level of spiking neurons to that of interacting cortical areas.

Materials & Methods

Mesoconnectome Construction

Neuron number

The number of neurons per layer follows from multiplying their volume density ρ_{neuron} with the layer thickness h_{layer} and the surface area A_{column} as $N_{\text{neuron}} = \rho_{\text{neuron}} h_{\text{layer}} A_{\text{column}}$. We use the volume density and the layer thickness provided in the seminal work of von Economo and Koskinas (***Von Economo, 2009***). This data distinguishes the layers into finer categories than the ones we use in our model. Therefore, we sum the corresponding "layer thickness overall" and average the corresponding "cell content" values weighted by the relative layer thickness.

Furthermore, the data is provided in the parcellation of von Economo and Koskinas; we use the mapping to the Desikan-Killiany parcellation constructed by ***Goulas et al.*** (***2016***, Table 1). In the given mapping, one or more von Economo and Koskinas areas are assigned to each Desikan-Killiany area. For the layer thicknesses, we take the average across the corresponding areas in the parcellation by von Economo and Koskinas (using that the mapping was constructed based on cytoarchitectonic similarity, such that the average is across architectonically similar areas); for the volume densities, we weight the average by the relative thickness of the layers.

To separate the neurons in a given layer into inhibitory and excitatory neurons, we use the layer-resolved relative size of the two populations from the electron-microscopy-based reconstruction of cortical tissue in the human temporal lobe by ***Shapson-Coe et al.*** (***2021***, Supplementary Figure 5B). The population sizes follow by multiplying the relative population size with the total number of neurons in the layer.

Fraction of Cortico-Cortical Connections

We separate the $N^{\text{cc}}_{\text{synapse}}$ cortico-cortical synapses from the $N^{1-\text{cc}}_{\text{synapse}} = N^{\text{total}}_{\text{synapse}} - N^{\text{cc}}_{\text{synapse}}$ synapses coming from within the area or from subcortical regions (see Data Aggregation and Predictive Connectomics). To determine the fraction of cortico-cortical synapses, we use the scaling rule by ***Herculano-Houzel et al.*** (***2010***),

$$\frac{N^{\text{cc}}_{\text{neuron}}}{N^{\text{total}}_{\text{neuron}}} \propto \frac{1}{\left(N^{\text{total}}_{\text{neuron}}\right)^{0.16}}; \tag{1}$$

i.e., the relative number of neurons connected through the white matter decreases with increasing total number of neurons in the gray matter $N^{\text{total}}_{\text{neuron}}$. We determine the proportionality constant

using the value $N^{\mathrm{cc}}_{\mathrm{neuron}}/N^{\mathrm{total}}_{\mathrm{neuron}} = 0.21$ from tracing data in macaque (***Markov et al., 2011***) in combination with 1.4×10^9 gray matter neurons in macaque (***Collins et al., 2010***). With the number of gray matter neurons in human, $N^{\mathrm{total}}_{\mathrm{neuron}} = 16 \times 10^9$ (***Herculano-Houzel, 2009***), we arrive at the estimate $N^{\mathrm{cc}}_{\mathrm{neuron}}/N^{\mathrm{total}}_{\mathrm{neuron}} = 0.14$ or $N^{1-\mathrm{cc}}_{\mathrm{neuron}}/N^{\mathrm{total}}_{\mathrm{neuron}} = 0.86$. Finally, we assume that the fraction of neurons connected through the white matter equals the fraction of cortico-cortical synapses.

Local Connectivity

The $N^{1-\mathrm{cc}}_{\mathrm{synapse}}$ local synapses need a further distinction: $N^{\mathrm{internal}}_{\mathrm{synapse}}$ synapses where the presynaptic neuron is part of the simulated column and $N^{\mathrm{external}}_{\mathrm{synapse}}$ synapses where the presynaptic neuron is outside of the simulated column, i.e., in the remainder of the area or in a subcortical region. To split these two categories, we use the spatial connection probability $p(\boldsymbol{x}_1 \mid \boldsymbol{x}_2)$ between a neuron located at $\boldsymbol{x}_1$ and another neuron at $\boldsymbol{x}_2$, which we assume to be a spatially homogeneous three-dimensional exponential distribution $p(\boldsymbol{x}_1 \mid \boldsymbol{x}_2) \propto \exp(-|\boldsymbol{x}_1 - \boldsymbol{x}_2|/\lambda_{\mathrm{conn}})$ with decay constant $\lambda_{\mathrm{conn}} = 160\,\mu\mathrm{m}$ (***Packer and Yuste, 2011***; ***Perin et al., 2011***). From $p(\boldsymbol{x}_1, \boldsymbol{x}_2) = p(\boldsymbol{x}_1 \mid \boldsymbol{x}_2)p(\boldsymbol{x}_2)$ where $p(\boldsymbol{x}_2)$ is assumed to be constant, we obtain the average connection probability P_{internal} within the column as

$$P_{\mathrm{internal}} \propto \int_{\mathrm{column}} d\boldsymbol{x}_1 \int_{\mathrm{column}} d\boldsymbol{x}_2 \, \exp(-|\boldsymbol{x}_1 - \boldsymbol{x}_2|/\lambda_{\mathrm{conn}}) \tag{2}$$

where the proportionality factor is the normalization constant of $p(\boldsymbol{x}_1, \boldsymbol{x}_2)$. We calculate the average connection probability assuming cylindrical columns. In cylindrical coordinates, using $d\boldsymbol{x} = r dr d\phi dz$ and $\int_0^a dx_1 \int_0^a dx_2 \, f(|x_2 - x_1|) = 2\int_0^a dy\,(a-y) f(|y|)$ simplifies this integral to

$$P_{\mathrm{internal}} \propto 4 \int_0^{r_{\mathrm{column}}} dr_1 \int_0^{r_{\mathrm{column}}} dr_2 \int_0^{2\pi} d\phi \int_0^h dz\, r_1 r_2 (2\pi - \phi)(h - z) \exp(-d(r_1, r_2, \phi, z)/\lambda_{\mathrm{conn}}) \tag{3}$$

with $d(r_1, r_2, \phi, z) = \sqrt{r_1^2 - 2r_1 r_2 \cos\phi + r_2^2 + z^2}$, the radius of the column r_{column}, and the total height of the column h. For the probability P_{external} that the postsynaptic neuron is in the column but the presynaptic neuron outside of it, the domain outside of the column has to be integrated: $\int_{\mathrm{column}} d\boldsymbol{x}_1 \to \int_{\neg\mathrm{column}} d\boldsymbol{x}_1$. Approximating the entire area as a cylinder, this leads to the replacement $\int_0^{r_{\mathrm{column}}} dr_1 \to \int_{r_{\mathrm{column}}}^{r_{\mathrm{area}}} dr_1$ where r_{area} is the radius of the larger cylinder, i.e.,

$$P_{\mathrm{external}} \propto 4 \int_{r_{\mathrm{column}}}^{r_{\mathrm{area}}} dr_1 \int_0^{r_{\mathrm{column}}} dr_2 \int_0^{2\pi} d\phi \int_0^h dz\, r_1 r_2 (2\pi - \phi)(h - z) \exp(-d(r_1, r_2, \phi, z)/\lambda_{\mathrm{conn}}). \tag{4}$$

The remaining integrals are solved numerically using the adaptive multidimensional quadrature implemented in SciPy (***Virtanen et al., 2020***). P_{internal} and P_{external} are used to determine the number of synapses with neurons within and outside of the column, respectively:

$$N^{\mathrm{internal}}_{\mathrm{synapse}} = \frac{P_{\mathrm{internal}}}{P_{\mathrm{internal}} + P_{\mathrm{external}}} N^{1-\mathrm{cc}}_{\mathrm{synapse}}, \tag{5}$$

$$N^{\mathrm{external}}_{\mathrm{synapse}} = \frac{P_{\mathrm{external}}}{P_{\mathrm{internal}} + P_{\mathrm{external}}} N^{1-\mathrm{cc}}_{\mathrm{synapse}}. \tag{6}$$

Note that although we keep r_{column} the same for all areas, both P_{internal} and P_{external} are area-specific because their thickness h and the neuron densities vary.

For the local connectivity within the column, comprising $N^{\mathrm{internal}}_{\mathrm{synapse}}$ synapses, we use the model of ***Potjans and Diesmann*** (***2014***) as a blueprint. More precisely, we use the average number of synapses $p^{\mathrm{PD}}_{\mathrm{B}\to\mathrm{A}}$ between a neuron in source population B and a neuron in target population A. We combine these average numbers of synapses with the number of neurons $N^{\mathrm{B}}_{\mathrm{neuron}}$, $N^{\mathrm{A}}_{\mathrm{neuron}}$ in the pre- and postsynaptic population:

$$N^{\mathrm{B}\to\mathrm{A}}_{\mathrm{synapse}} = \frac{N^{\mathrm{B}}_{\mathrm{neuron}} p^{\mathrm{PD}}_{\mathrm{B}\to\mathrm{A}} N^{\mathrm{A}}_{\mathrm{neuron}}}{\sum_{\mathrm{A,B}} N^{\mathrm{B}}_{\mathrm{neuron}} p^{\mathrm{PD}}_{\mathrm{B}\to\mathrm{A}} N^{\mathrm{A}}_{\mathrm{neuron}}} N^{\mathrm{internal}}_{\mathrm{synapse}}. \tag{7}$$

Eq. (7) keeps the average number of synapses per pair of neurons equal to the respective value in ***Potjans and Diesmann*** (***2014***) by construction.

The $N_{\text{synapse}}^{\text{external}}$ synapses from outside the column are also distributed based on ***Potjans and Diesmann*** (***2014***). Here, we use the indegrees $K_{\text{ext}\to\text{A}}^{\text{PD}}$ and the number of neurons in the postsynaptic population $N_{\text{neuron}}^{\text{A}}$:

$$N_{\text{synapse}}^{\text{ext}\to\text{A}} = \frac{K_{\text{ext}\to\text{A}}^{\text{PD}} N_{\text{neuron}}^{\text{A}}}{\sum_{\text{A}} K_{\text{ext}\to\text{A}}^{\text{PD}} N_{\text{neuron}}^{\text{A}}} N_{\text{synapse}}^{\text{external}}. \tag{8}$$

Both in Eq. (7) and Eq. (8), we round the final result to obtain an integer number of synapses.

Long-range projections

For the $N_{\text{synapse}}^{\text{cc}}$ synapses from other cortical areas, we assume that the presynaptic neurons are inside the simulated column in the respective presynaptic area. Thus, we do not distinguish between synapses with simulated and non-simulated presynaptic neurons—all presynaptic neurons of long-range projections are simulated.

We define the area-level connectivity according to processed DTI data from ***Goulas et al.*** (***2016***) which is based on data from the Human Connectome Project (***Van Essen et al., 2013***). For a given target area X, we distribute the synapses among the source areas based on the relative number of streamlines $\text{NoS}_{\text{Y}\to\text{X}}$ in the DTI data,

$$N_{\text{synapse}}^{\text{Y}\to\text{X}} = \frac{\text{NoS}_{\text{Y}\to\text{X}}}{\sum_{\text{Z}} \text{NoS}_{\text{Z}\to\text{X}}} N_{\text{synapse}}^{\text{cc}}. \tag{9}$$

Again, we round the resulting value.

A comprehensive dataset on the layer specificity of the presynaptic neurons based on retrograde tracing is available for macaque (***Markov et al., 2014b***,a). Not only in this species but also in cat, the layer specificity, i.e., the fraction of supragranular labeled neurons SLN, is systematically related to the cytoarchitecture (***van Albada et al., 2022***). For our human model, we assume the same quantitative relationship as in macaque. Fitting a beta-binomial model with a probit link function to the macaque data yields (***Schmidt et al., 2018a***)

$$\text{SLN}(\text{B}\to\text{A}) = \Phi\left(a_0 + a_1 \log(\rho_{\text{neuron}}^{\text{A}}/\rho_{\text{neuron}}^{\text{B}})\right) \tag{10}$$

where $\Phi(x) = \frac{1}{2}\left[1 + \text{erf}\left(x/\sqrt{2}\right)\right]$ denotes the cumulative distribution function of the standard normal distribution and the fitted parameters are $a_0 = -0.152$ and $a_1 = -1.534$. We use the human neuron densities in Eq. (10) to estimate the laminar origin in human. The SLN value allows determining whether the origin is in layer $2/3$ or not. Excluding layer 4, which does not form long-range projections (***Markov et al., 2014b***), the two infragranular layers 5 and 6 still need to be distinguished. To this end, we simply use the relative size of the two populations to distribute the remaining synapses.

On the target side, anterograde tracing can specify the layer specificity. However, there are no comprehensive datasets of anterograde tracing in non-human primates available to date. Hence, we use the collected data from the CoCoMac database (***Stephan et al., 2001***) which aggregates data across many tracing studies. Relating the target patterns from anterograde tracing to the SLN value reveals three categories of target patterns (***Schmidt et al., 2018a***):

$$\begin{aligned} \text{SLN} > 65\% &: [4] \\ 35\% \leq \text{SLN} \leq 65\% &: [1, 2/3, 4, 5, 6] \\ \text{SLN} < 35\% &: [1, 2/3, 5, 6] \end{aligned}$$

where layer 4 is replaced by $2/3$ in the first case for agranular target areas (***Beul and Hilgetag, 2015***). Using the SLN value to distinguish feedforward ($\text{SLN} > 65\%$), lateral ($35\% \leq \text{SLN} \leq 65\%$), and feedback ($\text{SLN} < 35\%$) connections, this implies that feedforward connections target layer 4, feedback connections avoid layer 4, and lateral connections show no distinct pattern. For the quantitative distribution of the synapses onto the layers included in the respective target pattern, we use the relative thickness of the layer in relation to all layers of the target pattern.

Thus far, we determined the location of the synapse in the target layer. Next, we decide whether the postsynaptic neuron of a synapse in a given layer is excitatory or inhibitory based on the analysis of the data by ***Binzegger et al.*** (***2004***) in ***Schmidt et al.*** (***2018a***, Table S11). To this end, we sum the target probabilities for postsynaptic neurons across all layers separately for excitatory and inhibitory neurons. This yields the probability for a synapse in a given layer to have an excitatory or inhibitory postsynaptic neuron in any layer. However, we take one exception into account: For feedback connections ($\mathrm{SLN} < 35\%$), we fix the fraction of excitatory target cells to 93% (***Schmidt et al., 2018a***) because feedback connections preferentially target excitatory neurons (***Johnson and Burkhalter, 1996***; ***Anderson et al., 2011***).

To finally determine the postsynaptic neuron, we assume that all inhibitory postsynaptic neurons are in the same layer as the synapse. For the excitatory neurons, we take the dendritic morphology into account. Using morphological reconstructions of human pyramidal cells in temporal cortex (***Mohan et al., 2015***), we calculate the layer-resolved length of dendrites for neurons with the soma in a given layer. Assuming a constant density of synapses along the dendrites, the ratio of the length $\ell_{\mathrm{A,B}}$ of dendrites in layer $\mathrm{A} \in [1, 2/3, 4, 5, 6]$ belonging to a neuron with soma in layer $\mathrm{B} \in [2/3, 4, 5, 6]$ to the total length of dendrites in this layer, $\sum_{\mathrm{B}} \ell_{\mathrm{A,B}}$, determines the probability that the postsynaptic cell is in layer B given that the synapse is in layer A: $P(\text{soma in B} \mid \text{synapse in A}) = \ell_{\mathrm{A,B}} / \sum_{\mathrm{B}} \ell_{\mathrm{A,B}}$.

Ultimately, we only need the location of the postsynaptic neuron but not the location of the synapse. Thus, we multiply $P(\text{soma in B} \mid \text{synapse in A})$ with the distribution of the synapses across the layers and marginalize the synapse location.

Further Parameters of the Model

Neuron parameters

We use the leaky integrate-and-fire (LIF) neuron model with exponential postsynaptic currents (***Gerstner et al., 2014***) for all neurons. To determine the parameter values, we analyzed the LIF models from the Allen Cell Types Database (https://celltypes.brain-map.org/; ***Teeter et al., 2018***; ***Berg et al., 2021***) which were fitted to human neurons. For both excitatory and inhibitory cells, we fix the leak and reset potential to $\mathrm{V_L} = \mathrm{V_{reset}} = -70\,\mathrm{mV}$. For the threshold potential $\mathrm{V_{th}}$, the membrane time constant τ_{m}, and the membrane capacitance $\mathrm{C_m}$, we fitted a log-normal distribution using maximum likelihood estimation to the distribution of the respective parameter for all cells in which the LIF model had an explained variance above 0.75 to ensure a good fit of the LIF model. For convenience, we parameterize the log-normal distribution using the mean and the coefficient of variation CV. The resulting mean threshold potential is $\mathrm{V_{th}} = -45\,\mathrm{mV}$ for both excitatory and inhibitory cells with $\mathrm{CV} = 0.21$ and $\mathrm{CV} = 0.22$ for excitatory and inhibitory cells, respectively. The resulting mean capacitance is $\mathrm{C_m} = 220\,\mathrm{pF}$ and $\mathrm{C_m} = 100\,\mathrm{pF}$ with $\mathrm{CV} = 0.22$ and $\mathrm{CV} = 0.34$ for excitatory and inhibitory cells, respectively. To account for the high conductance state in vivo (***Destexhe et al., 2003***), we lower the membrane time constant to $\tau_{\mathrm{m}} = 10\,\mathrm{ms}$ on average with $\mathrm{CV} = 0.55$ and $\mathrm{CV} = 0.43$ for excitatory and inhibitory cells, respectively. We do not distribute the synaptic time constants, which we fix to $\tau_{\mathrm{s}} = 2\,\mathrm{ms}$, and the absolute refractory period of $\mathrm{t_{ref}} = 2\,\mathrm{ms}$.

In all simulations shown in the main text, the neuron parameters are not distributed, i.e., all coefficients of variation were set to $\mathrm{CV} = 0$. Simulations with distributed neuron parameters are shown in the appendix.

Synapse parameters

We use static synapses with a transmission probability of $100\,\%$. Excitatory postsynaptic potentials follow a truncated normal distribution with average $0.1\,\mathrm{mV}$ and relative standard deviation of $10\,\%$. The inhibitory postsynaptic potentials also follow a truncated normal distribution with a factor $g = 5$ larger absolute value of the mean and standard deviation. Excitatory (inhibitory) weights are truncated below (above) zero; values outside of the allowed range are redrawn.

Post-synaptic potentials are converted into post-synaptic currents using the conversion factor

$$\frac{\mathrm{PSC}}{\mathrm{PSP}} = \frac{C_\mathrm{m}}{\tau_\mathrm{m}} \epsilon^{-1/(1-\epsilon)}, \qquad \epsilon = \frac{\tau_\mathrm{s}}{\tau_\mathrm{m}}. \tag{11}$$

Note that the conversion factor depends on both the synapse parameters (τ_s) and the post-synaptic neuron parameters (τ_m, C_m).

We introduce several scaling factors that affect the postsynaptic potentials: First, the synaptic weights of the synapses within a column from layer IV excitatory neurons to layer II/III excitatory neurons are increased twofold in agreement with the blueprint (***Potjans and Diesmann, 2014***). Second, we introduce a scaling factor χ_I for the cortico-cortical synapses targeting inhibitory neurons. This scaling factor stabilizes the column with respect to cortico-cortical input. For all simulations shown, it is set to 2.0. Third, we introduce a scaling factor χ for the cortico-cortical connections onto both excitatory and inhibitory neurons. Increasing this factor leads to the best-fit state reported in Fig. 5 and Fig. 6. For cortico-cortical synapses onto inhibitory neurons χ_I and χ are multiplied.

Delays

Within a column, the average delay is $1.5\,\mathrm{ms}$ for excitatory and $0.75\,\mathrm{ms}$ for inhibitory synapses. For the cortico-cortical synapses, we assume a conduction velocity of $3.5\,\mathrm{m/s}$ (***Girard et al., 2001***). Dividing the fiber length between two areas, obtained through tractography (***Goulas et al., 2016***), by the conduction velocity, we obtain the average delay between the two areas. All delays follow a truncated log-normal distribution with a relative standard deviation of $50\,\%$. Delays are truncated below the resolution of the simulation; values outside of the allowed range are redrawn.

External input

We determined the number of synapses from non-simulated presynaptic neurons in Eq. (8). The postsynaptic potentials follow a truncated normal distribution with average $\mathrm{w}_\mathrm{ext} = 0.1\,\mathrm{mV}$ and relative standard deviation of $10\,\%$. We keep the mean input, measured relative to rheobase, fixed at $\eta_\mathrm{ext} = 1.1$ and determine the rate of the driving Poisson processes by

$$\nu_\mathrm{ext}^\mathrm{A} = \frac{\mathrm{V_{th}} - \mathrm{V_L}}{\tau_\mathrm{m} \mathrm{w}_\mathrm{ext} K_\mathrm{A}^\mathrm{ext}} \eta_\mathrm{ext} \tag{12}$$

with $K_\mathrm{A}^\mathrm{ext} = N_\mathrm{synapse}^{\mathrm{ext}\to\mathrm{A}} / N_\mathrm{neuron}^\mathrm{A}$. We further introduce two scaling factors for the postsynaptic potentials arriving at excitatory neurons in layer 5 and 6, respectively. For all simulations shown, the first scaling factor is set to 1.05 and the second to 1.15.

Model summary	
Populations	254 populations: 34 areas (Table 1) with eight populations each (areas caudalanteriorcingulate, caudalmiddlefrontal, entorhinal, lateraloccipital, parahippocampal, parsorbitalis, precentral, rostralanteriorcingulate have six). The model consists of about 3.5 million neurons and 43 billion synapses.
Topology	—
Connectivity	area- and population-specific but otherwise random
Neuron model	leaky integrate-and-fire (LIF), fixed absolute refractory period (voltage clamp)
Synapse model	exponential postsynaptic currents
Plasticity	—
Input	independent homogeneous Poisson spike trains
Measurements	spiking activity
Populations	
Type	Cortex
Elements	LIF neurons
Number of populations	34 areas with eight populations each (areas caudalanteriorcingulate, caudalmiddlefrontal, entorhinal, lateraloccipital, parahippocampal, parsorbitalis, precentral, rostralanteriorcingulate have six), two per layer
Population size	N (area- and population-specific)
Connectivity	
Type	source and target neurons drawn randomly with replacement (allowing autapses and multapses) with area- and population-specific connection probabilities. The total number of synapses between populations is fixed, corresponding to the "Random, fixed total number" rule described by ***Senk et al.*** (***2022***).
Weights	fixed, drawn from normal distribution with mean J such that postsynaptic potentials have a mean amplitude of $0.1\,\mathrm{mV}$ and standard deviation $\delta J = 0.1J$; 4E to 2/3E (cf. ***Potjans and Diesmann, 2014***) increased by factor 2; weights of inhibitory connections increased by factor g; excitatory weights < 0 and inhibitory weights > 0 are redrawn; cortico-cortical weights onto inhibitory populations increased by factor χ_I and onto excitatory and inhibitory populations increased by factor χ
Delays	fixed, drawn from clipped lognormal distribution with mean d and standard deviation $\delta d = 0.5d$; delays of inhibitory connections factor 2 smaller; delays rounded to the nearest multiple of the simulation step size $h = 0.1\,\mathrm{ms}$, inter-area delays drawn from a Gaussian distribution with mean $d = s/v_\mathrm{t}$, with distance s and transmission speed $v_\mathrm{t} = 3.5\,\mathrm{m/s}$ (***Girard et al., 2001***); and standard deviation $\delta d = d/2$, distances determined as the median of the distances between all vertex pairs of the two areas in the DTI data (***Goulas et al., 2016***), delays $< 0.1\,\mathrm{ms}$ before rounding are redrawn
Neuron and synapse model	
Name	LIF neuron
Type	leaky integrate-and-fire, exponential synaptic current inputs
Subthreshold dynamics	$\frac{dV}{dt} = -\frac{V-E_\mathrm{L}}{\tau_\mathrm{m}} + \frac{I_\mathrm{s}(t)}{C_\mathrm{m}}$, if$(t > t^* + \tau_\mathrm{r})$ $V(t) = V_\mathrm{r}$, else $I_\mathrm{s}(t) = \sum_{i,k} J_k\, e^{-(t-t_i^k)/\tau_\mathrm{s}} \Theta(t - t_i^k)$, k: neuron index, i: spike index
Spiking	If $V(t-) < \theta \wedge V(t+) \geq \theta$ 1. set $t^* = t$, 2. emit spike with time stamp t^*
Input	
Type	Background
Target	LIF neurons
Description	Independent homogeneous Poisson spike trains to all neurons in the network; rate fixed such that the mean input, measured relative to rheobase, is $\eta_\mathrm{ext} = 1.1$
Measurements	
	Spiking activity

Table 2. Model description after ***Nordlie et al.*** (***2009***).

Synapse parameters		
Name	**Value**	**Description**
$J \pm \delta J$	Intra-areal connections: 16.4 ± 1.6 pA onto excitatory and 7.5 ± 0.8 pA onto inhibitory neurons prior to the application of scaling factors, cortico-cortical connections scaled as $J_{cc} = \chi J$ onto excitatory and $J_{cc} = \chi \chi_I J$ onto inhibitory neurons	excitatory synaptic strength
g	$g = 5$	relative inhibitory synaptic strength
$d_e \pm \delta d_e$	1.5 ± 0.75 ms	local excitatory transmission delay
$d_i \pm \delta d_i$	0.75 ± 0.375 ms	local inhibitory transmission delay
$d \pm \delta d$	$d = s/v_t \pm \frac{1}{2} s/v_t$	inter-area transmission delay, with s the distance between areas
v_t	3.5 m/s	transmission speed
Neuron parameters		
Name	**Value**	**Description**
τ_m	10 ms	membrane time constant
τ_r	2 ms	absolute refractory period
τ_s	2 ms	postsynaptic current time constant
C_m	220 pF for excitatory neurons, 100 pF for inhibitory neurons	membrane capacity
V_r	-70 mV	reset potential
θ	-45 mV	fixed firing threshold
E_L	-70 mV	leak potential

Table 3. Parameter specification for synapses and neurons.

Activity Data

Spiking data

Minxha et al. (***2020***) recorded from thirteen adult epilepsy patients under evaluation for surgical treatment using depth electrodes in medial frontal cortex. In total, they recorded 767 neurons within 320 trials and extracted spikes using a semi-automated spike sorting algorithm. For our analysis, we disregard task-related activity and use only the two seconds of activity which were recorded before stimulus onset. The data is publicly available via the Open Science Framework at http://doi.org/10.17605/OSF.IO/U3KCP.

fMRI data

Participants

Nineteen participants (7 female, age range = 21–33 years, mean age = 25 years) with normal or corrected-to-normal visual acuity took part in this study. All participants provided written informed consent after receiving full information about experimental procedures and were compensated for participation either through monetary reward or course credit. All procedures were conducted with approval from the local Ethical Committee of the Faculty of Psychology and Neuroscience at Maastricht University.

Magnetic resonance imaging

Anatomical and functional images were acquired at Maastricht Brain Imaging Centre (Maastricht University) on a whole-body Magnetom 7T research scanner (Siemens Healthineers, Erlangen, Germany) using a 32-channel head-coil (Nova Medical Inc.; Wilmington, MA, USA). Anatomical data were collected prior to functional data with an MP2RAGE (***Marques et al., 2010***) imaging sequence [240 slices, matrix = 320×320, voxel size = $0.65 \times 0.65 \times 0.65$ mm^3, first inversion time (TI1) = 900 ms,

second inversion time (TI2) = $2750\,\mathrm{ms}$, echo time (TE) = $2.51\,\mathrm{ms}$, repetition time (TR) = $5000\,\mathrm{ms}$, first nominal flip angle = 5°, and second nominal flip angle = 3°, GRAPPA = 2]. Functional images were acquired using a gradient-echo echo-planar (***Moeller et al., 2010***) imaging sequence (84 slices, matrix = 186×186, voxel size = $1,6 \times 1.6 \times 1.6\ \mathrm{mm}^3$, TE = $22\,\mathrm{ms}$, TR = $1500\,\mathrm{ms}$, nominal flip angle = 63°, GRAPPA = 2, multi-band factor = 4). In addition, after the first functional run, we recorded five functional volumes with opposed phase encoding directions to correct for EPI distortions that occur at higher field strengths (***Andersson et al., 2003***).

Participants underwent five functional runs comprising of a resting-state measurement, three individual task measurements and a task-switching paradigm wherein participants repeatedly performed each of the three tasks. With the exception of the task-switching run, which lasted $9.5\,\mathrm{min}$, all functional runs lasted $15\,\mathrm{min}$. Since task-related runs were not included in the present study, they will not be discussed further. However, it is noteworthy that resting-state runs always preceded task-related runs to prevent carry-over effects (***Grigg and Grady, 2010***). Participants were instructed to close their eyes during resting-state runs and otherwise to let their mind wander freely.

Processing of (f)MRI data

Anatomical images were downsampled to $0.8 \times 0.8 \times 0.8\ \mathrm{mm}^3$ and subsequently automatically processed with the longitudinal stream in FreeSurfer (http://surfer.nmr.mgh.harvard.edu/) including probabilistic atlas-based cortical parcellation according to the Desikan-Killiany (DK) atlas (***Desikan et al., 2006***). Initial preprocessing of functional data was performed in BrainVoyager 20 (version 20.0; Brain Innovation; Maastricht, The Netherlands) and included slice scan time correction and (rigid body) motion correction wherein all functional runs were aligned to the first volume of the first functional run. EPI distortions were then corrected using the COPE ("Correction based on Opposite Phase Encoding") plugin of BrainVoyager that implements a method similar to that described in ***Andersson et al.*** (***2003***) and the 'topup' tool implemented in FSL (***Smith et al., 2004***). The pairs of reversed phase encoding images recorded in the beginning of the scanning session were used to estimate the susceptibility-induced off-resonance field and correct the distortions in the remaining functional runs. This was followed by wavelet despiking (***Patel and Bullmore, 2016***) using the BrainWavelet Toolbox (brainwavelet.org) for MATLAB (2019a, The MathWorks,Natick, MA). Subsequently, high-pass filtering was performed in BrainVoyager with a frequency cutoff of $0.01\,\mathrm{Hz}$ and to register functional images to participants' anatomical images. Using MATLAB, functional data were then cleaned further by regressing out a global noise signal given by the first five principal components of signals observed within the cerebrospinal fluid of the ventricles (***Behzadi et al., 2007***). Finally, voxels were uniquely assigned to one of 68 cortical regions of interest (ROIs) and an average blood-oxygen-level-dependent (BOLD) signal for each ROI was obtained as the mean of the time-series of its constituent voxels.

Mean-Field Theory

While developing the model, it was often beneficial to have a prediction of the activity without performing a computationally demanding full-scale simulation. To this end, we employed the mean-field theory developed in ***Amit and Brunel*** (***1997***) in combination with the extension to exponential post-synaptic currents derived in ***Fourcaud and Brunel*** (***2002***). Within this theory, the input to a neuron in population A is approximated as a Gaussian white noise with mean μ_A and noise intensity σ_A^2. The main assumptions of this theory are that the inputs are uncorrelated, that the temporal structure of the input can be neglected, that a Gaussian approximation of its statistics is valid, that the delays can be neglected, and that the variability of the neuron parameters and synaptic weights can be neglected.

Despite the simplifying assumptions, the theory provides a reliable prediction of the average firing rates if the network is in an asynchronous irregular state (Fig. 8). The remaining deviations are likely a consequence of the neglected variabilities, in particular the distributed neuron parameters.

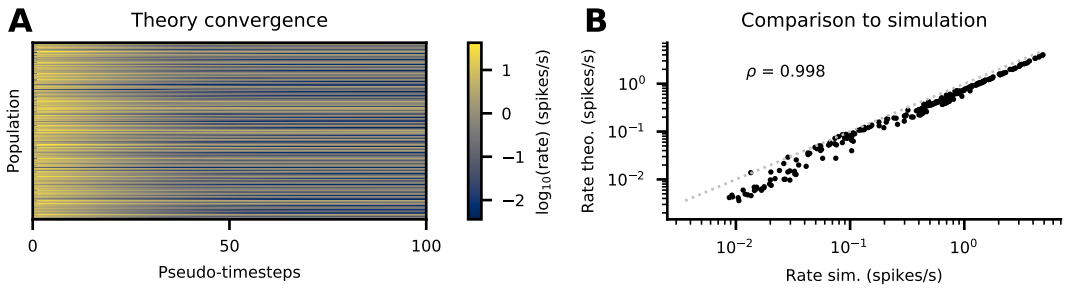

Figure 8. Mean-field theory. (**A**) Firing rates of all populations across the pseudo-timesteps used to find a self-consistent solution. (**B**) Comparison with rates predicted by mean-field theory to empirical rates from a simulation.

Thus, the theory allows for rapid prototyping without the need for high performance computing resources.

Code & Workflow

The entire workflow of the model, from data preprocessing through the simulation to the final analysis, relies on the Python programming language (***Python Software Foundation, 2008***) version 3.6.5 in combination with NumPy (***Harris et al., 2020***) version 1.14.3, SciPy (***Virtanen et al., 2020***) version 1.1.0, pandas (***Wes McKinney, 2010***) version 0.23.4, Matplotlib (***Hunter, 2007***) version 2.2.2, networkx version 2.4 (***Hagberg et al., 2008***), and seaborn (***Waskom, 2021***) version 0.9.0. All simulations were performed using the NEST simulator (***Gewaltig and Diesmann, 2007***) version 2.20.2 (***Fardet et al., 2021***) on the JURECA-DC supercomputer. The workflow is structured using snakemake (***Köster and Rahmann, 2012***). For the mean-field analysis, we used the NNMT toolbox (***Layer et al., 2022***).

Acknowledgments

We thank Sebastian Bludau and Timo Dickscheid for helpful discussions about cytoarchitecture and parcellations. Furthermore, we gratefully acknowledge all the shared experimental data that underlies our work, and the effort spent to collect it.

This work was supported by the German Research Foundation (DFG) Priority Program "Computational Connectomics" (SPP 2041; Project 347572269), the European Union's Horizon 2020 Framework Programme for Research and Innovation under Specific Grant Agreement No. 945539 (Human Brain Project SGA3), the Helmholtz Association through the Helmholtz Portfolio Theme "Supercomputing and Modeling for the Human Brain", and HiRSE_PS, the Helmholtz Platform for Research Software Engineering - Preparatory Study, an innovation pool project of the Helmholtz Association. The use of the JURECA-DC supercomputer in Jülich was made possible through VSR computation time grant JINB33 ("Brain-Scale Simulations").

References

van Albada SJ, Morales-Gregorio A, Dickscheid T, Goulas A, Bakker R, Bludau S, Palm G, Hilgetag CC, Diesmann M. Bringing Anatomical Information into Neuronal Network Models. In: Giugliano M, Negrello M, Linaro D, editors. *Computational Modelling of the Brain: Modelling Approaches to Cells, Circuits and Networks* Cham: Springer International Publishing; 2022.p. 201–234. doi: 10.1007/978-3-030-89439-9_9.

van Albada SJ, Pronold J, van Meegen A, Diesmann M. Usage and Scaling of an Open-Source Spiking Multi-Area Model of Monkey Cortex. In: *Lecture Notes in Computer Science* Springer International Publishing; 2021.p. 47–59. https://doi.org/10.1007/978-3-030-82427-3_4, doi: 10.1007/978-3-030-82427-3_4.

van Albada SJ, Helias M, Diesmann M. Scalability of Asynchronous Networks Is Limited by One-to-One Mapping between Effective Connectivity and Correlations. PLOS Comput Biol. 2015; 11(9):e1004490. https://doi.org/10.1371/journal.pcbi.1004490, doi: 10.1371/journal.pcbi.1004490.

Albers J, Pronold J, Kurth AC, Vennemo S, Haghighi Mood K, Patronis A, Terhorst D, Jordan J, Kunkel S, Tetzlaff T, Diesmann M, Senk J. A Modular Workflow for Performance Benchmarking of Neuronal Network Simulations. Front Neuroinform. 2022; 16:837549. doi: 10.3389/fninf.2022.837549.

Alkemade A, Bazin PL, Balesar R, Pine K, Kirilina E, Möller HE, Trampel R, Kros JM, Keuken MC, Bleys RL, et al. A unified 3D map of microscopic architecture and MRI of the human brain. Science Advances. 2022; 8(17):eabj7892.

Amit DJ, Brunel N. Model of Global Spontaneous Activity and Local Structured Activity During Delay periods in the Cerebral Cortex. Cereb Cortex. 1997 Apr; 7:237–252. https://doi.org/10.1093/cercor/7.3.237, doi: 10.1093/cercor/7.3.237.

Amunts K, Lepage C, Borgeat L, Mohlberg H, Dickscheid T, Rousseau MÉ, Bludau S, Bazin PL, Lewis LB, Oros-Peusquens AM, et al. BigBrain: an ultrahigh-resolution 3D human brain model. Science. 2013; 340(6139):1472–1475.

Amunts K, Mohlberg H, Bludau S, Zilles K. Julich-Brain: A 3D probabilistic atlas of the human brain's cytoarchitecture. Science. 2020; 369(6506):988–992. doi: 10.1126/science.abb4588.

Anderson JC, Kennedy H, Martin KAC. Pathways of Attention: Synaptic Relationships of Frontal Eye Field to V4, Lateral Intraparietal Cortex, and Area 46 in Macaque Monkey. J Neurosci. 2011; 31(30):10872–10881. http://www.jneurosci.org/content/31/30/10872.abstract, doi: 10.1523/JNEUROSCI.0622-11.2011.

Anderson JC, Martin KAC. The Synaptic Connections between Cortical Areas V1 and V2 in Macaque Monkey. J Neurosci. 2009; 29(36):11283–11293.

Andersson JLR, Skare S, Ashburner J. How to correct susceptibility distortions in spin-echo echo-planar images: application to diffusion tensor imaging. Neuroimage. 2003; 20(2):870–888. https://www.sciencedirect.com/science/article/pii/S1053811903003367, doi: 10.1016/S1053-8119(03)00336-7.

Angulo M, Rossier J, Audinat E. Postsynaptic glutamate receptors and integrative properties of fast- spiking interneurons in the rat neocortex. J Neurophysiol. 1999 Sep; 82(3):1295–302.

Arkhipov A, Gouwens NW, Billeh YN, Gratiy S, Iyer R, Wei Z, Xu Z, Abbasi-Asl R, Berg J, Buice M, et al. Visual physiology of the layer 4 cortical circuit in silico. PLOS Comput Biol. 2018; 14(11):e1006535. doi: 10.1371/journal.pcbi.1006535.

Bakker R, Thomas W, Diesmann M. CoCoMac 2.0 and the future of tract-tracing databases. Front Neuroinform. 2012; 6:30. doi: 10.3389/fninf.2012.00030.

Barbas H, Rempel-Clower N. Cortical structure predicts the pattern of corticocortical connections. Cereb Cortex. 1997; 7(7):635–646. http://cercor.oxfordjournals.org/content/7/7/635.abstract, doi: 10.1093/cercor/7.7.635.

Bassett DS, Bullmore ET. Small-world brain networks revisited. Neuroscientist. 2017; 23(5):499–516. doi: 10.1177/1073858416667720.

Behzadi Y, Restom K, Liau J, Liu TT. A component based noise correction method (CompCor) for BOLD and perfusion based fMRI. Neuroimage. 2007; 37(1):90–101. https://www.sciencedirect.com/science/article/pii/S1053811907003837, doi: j.neuroimage.2007.04.042.

Berg J, Sorensen SA, Ting JT, Miller JA, Chartrand T, Buchin A, Bakken TE, Budzillo A, Dee N, Ding SL, Gouwens NW, Hodge RD, Kalmbach B, Lee C, Lee BR, Alfiler L, Baker K, Barkan E, Beller A, Berry K, et al. Human neocortical expansion involves glutamatergic neuron diversification. Nature. 2021 Oct; 598(7879):151–158. doi: 10.1038/s41586-021-03813-8.

Beul SF, Barbas H, Hilgetag CC. A predictive structural model of the primate connectome. Sci Rep. 2017; 7(43176):1–12. doi: 10.1038/srep43176.

Beul SF, Hilgetag CC. Towards a 'canonical' agranular cortical microcircuit. Front Neuroanat. 2015; 8:165. http://www.frontiersin.org/neuroanatomy/10.3389/fnana.2014.00165/abstract, doi: 10.3389/fnana.2014.00165.

Bezaire MJ, Raikov I, Burk K, Vyas D, Soltesz I. Interneuronal mechanisms of hippocampal theta oscillations in a full-scale model of the rodent CA1 circuit. eLife. 2016 Dec; 5. https://doi.org/10.7554/elife.18566, doi: 10.7554/elife.18566.

Billeh YN, Cai B, Gratiy SL, Dai K, Iyer R, Gouwens NW, Abbasi-Asl R, Jia X, Siegle JH, Olsen SR, et al. Systematic integration of structural and functional data into multi-scale models of mouse primary visual cortex. Neuron. 2020; 106(3):388–403.e18. https://www.sciencedirect.com/science/article/pii/S0896627320300672, doi: https://doi.org/10.1016/j.neuron.2020.01.040.

Binzegger T, Douglas RJ, Martin KAC. A Quantitative Map of the Circuit of Cat Primary Visual Cortex. J Neurosci. 2004; 39(24):8441–8453. https://doi.org/10.1523/jneurosci.1400-04.2004, doi: 10.1523/JNEUROSCI.1400-04.2004.

Brecht M, Schneider M, Sakmann B, Margrie TW. Whisker movements evoked by stimulation of single pyramidal cells in rat motor cortex. Nature. 2004; 427(6976):704–710. doi: 10.1038/nature02266.

Campagnola L, Seeman SC, Chartrand T, Kim L, Hoggarth A, Gamlin C, Ito S, Trinh J, Davoudian P, Radaelli C, et al. Local connectivity and synaptic dynamics in mouse and human neocortex. Science. 2022; 375(6585):eabj5861.

Cano-Astorga N, DeFelipe J, Alonso-Nanclares L. Three-Dimensional Synaptic Organization of Layer III of the Human Temporal Neocortex. Cereb Cortex. 2021; 31(10):4742–4764. doi: 10.1093/cercor/bhab120.

Casali S, Marenzi E, Medini KC, Casellato C, D'Angelo E. Reconstruction and simulation of a scaffold model of the cerebellar network. Front Neuroinform. 2019; 13:37.

Collins CE, Airey DC, Young NA, Leitch DB, Kaas JH. Neuron densities vary across and within cortical areas in primates. Proc Natl Acad Sci USA. 2010 September; 107(36):15927–15932. doi: 10.1073/pnas.1010356107.

Deco G, Jirsa VK, McIntosh AR. Emerging concepts for the dynamical organization of resting-state activity in the brain. Nat Rev Neurosci. 2011; 12:43–56. doi: 10.1038/nrn2961.

Deco G, Jirsa VK, Robinson PA, Breakspear M, Friston K. The Dynamic Brain: From Spiking Neurons to Neural Masses and Cortical Fields. PLOS Comput Biol. 2008 Aug; 4(8):e1000092. https://doi.org/10.1371/journal.pcbi.1000092, doi: 10.1371/journal.pcbi.1000092.

DeFelipe J, Alonso-Nanclares L, Arellano JI. Microstructure of the neocortex: comparative aspects. J Neurocytol. 2002; 31:299–316. https://doi.org/10.1023/A:1024130211265, doi: 10.1023/A:1024130211265.

DeFelipe J, Elston G, Fujita I, Fuster J, Harrison K, Hof P, Kawaguchi Y, Martin K, Rockland K, Thomson A, Wang S, White E, Yuste R. Neocortical circuits: Evolutionary aspects and specificity versus non-specificity of synaptic connections. Remarks, main conclusions and general comments and discussion. J Neurocytol. 2002; 32:387–416. https://doi.org/10.1023/A:1024142513991, doi: 10.1023/A:1024142513991.

Dentico D, Cheung BL, Chang JY, Guokas J, Boly M, Tononi G, Van Veen B. Reversal of cortical information flow during visual imagery as compared to visual perception. Neuroimage. 2014; 100:237–243. http://www.sciencedirect.com/science/article/pii/S1053811914004662, doi: http://doi.org/10.1016/j.neuroimage.2014.05.081.

Desikan RS, Ségonne F, Fischl B, Quinn BT, Dickerson BC, Blacker D, Buckner RL, Dale AM, Maguire RP, Hyman BT, Albert MS, Killiany RJ. An automated labeling system for subdividing the human cerebral cortex on MRI scans into gyral based regions of interest. Neuroimage. 2006; 31(3):968–980. https://www.sciencedirect.com/science/article/pii/S1053811906000437, doi: 10.1016/j.neuroimage.2006.01.021.

Destexhe A, Rudolph M, Pare D. The high-conductance state of neocortical neurons in vivo. Nat Rev Neurosci. 2003; 4:739–751. doi: 10.1038/nrn1198.

Diesmann M, Gewaltig MO. NEST: An Environment for Neural Systems Simulations. In: Plesser T, Macho V, editors. *Forschung und wisschenschaftliches Rechnen, Beiträge zum Heinz-Billing-Preis 2001*, vol. 58 of GWDG-Bericht Göttingen: Ges. für Wiss. Datenverarbeitung; 2002.p. 43–70.

Dijkstra EW. A note on two problems in connexion with graphs. Numer Math. 1959; 1(1):269–271. http://doi.org/10.1007/BF01386390, doi: 10.1007/BF01386390.

Ecker A, Romani A, Sáray S, Káli S, Migliore M, Falck J, Lange S, Mercer A, Thomson AM, Muller E, Reimann MW, Ramaswamy S. Data-driven integration of hippocampal CA1 synaptic physiology in silico. Hippocampus. 2020 Jun; 30(11):1129–1145. https://doi.org/10.1002/hipo.23220, doi: 10.1002/hipo.23220.

Einevoll GT, Destexhe A, Diesmann M, Grün S, Jirsa V, de Kamps M, Migliore M, Ness TV, Plesser HE, Schürmann F. The Scientific Case for Brain Simulations. Neuron. 2019; 102(4):735–744. https://www.sciencedirect.com/science/article/pii/S0896627319302909, doi: 10.1016/j.neuron.2019.03.027.

Ercsey-Ravasz M, Markov NT, Lamy C, Essen DCV, Knoblauch K, Toroczkai Z, Kennedy H. A Predictive Network Model of Cerebral Cortical Connectivity Based on a Distance Rule. Neuron. 2013; 80(1):184–197. doi: 10.1016/j.neuron.2013.07.036.

Fardet T, Vennemo SB, Mitchell J, Mørk H, Graber S, Hahne J, Spreizer S, Deepu R, Trensch G, Weidel P, Jordan J, Eppler JM, Terhorst D, Morrison A, Linssen C, Antonietti A, Dai K, Serenko A, Cai B, Kubaj P, et al., NEST 2.20.2. Zenodo; 2021. https://doi.org/10.5281/zenodo.5242954, doi: 10.5281/zenodo.5242954.

Fourcaud N, Brunel N. Dynamics of the firing probability of noisy integrate-and-fire neurons. Neural Comput. 2002; 14:2057–2110. https://doi.org/10.1162/089976602320264015, doi: 10.1162/089976602320264015.

Gămănuţ R, Kennedy H, Toroczkai Z, Ercsey-Ravasz M, Van Essen DC, Knoblauch K, Burkhalter A. The mouse cortical connectome, characterized by an ultra-dense cortical graph, maintains specificity by distinct connectivity profiles. Neuron. 2018; 97(3):698–715. doi: 10.1016/j.neuron.2017.12.037.

Gerstner W, Kistler WM, Naud R, Paninski L. Neuronal Dynamics. From Single Neurons to Networks and Models of Cognition. Cambridge: Cambridge University Press; 2014. doi: 10.1017/cbo9781107447615.

Gewaltig MO, Diesmann M. NEST (NEural Simulation Tool). Scholarpedia J. 2007; 2(4):1430. https://doi.org/10.4249/scholarpedia.1430, doi: 10.4249/scholarpedia.1430.

Girard P, Hupé JM, Bullier J. Feedforward and Feedback Connections Between Areas V1 and V2 of the Monkey Have Similar Rapid Conduction Velocities. J Neurophysiol. 2001; 85(3):1328–1331. doi: 10.1152/jn.2001.85.3.1328.

Girardi-Schappo M, Bortolotto GS, Gonsalves JJ, Pinto LT, Tragtenberg MHR. Griffiths phase and long-range correlations in a biologically motivated visual cortex model. Sci Rep. 2016 Jul; 6(1). https://doi.org/10.1038/srep29561, doi: 10.1038/srep29561.

Goulas A, Werner R, Beul SF, Säring D, Heuvel Mvd, Triarhou LC, Hilgetag CC. Cytoarchitectonic similarity is a wiring principle of the human connectome. BioRxiv. 2016; doi: 10.1101/068254.

Grigg O, Grady CL. Task-Related Effects on the Temporal and Spatial Dynamics of Resting-State Functional Connectivity in the Default Network. PLOSONE. 2010 10; 5(10):1–12. https://doi.org/10.1371/journal.pone.0013311, doi: 10.1371/journal.pone.0013311.

Gupta A, Wang Y, Markram H. Organizing Principles for a Diversity of GABAergic Interneurons and Synapses in the Neocortex. Science. 2000; 287:273–278.

Hagberg AA, Schult DA, Swart PJ. Exploring Network Structure, Dynamics, and Function using NetworkX. In: Varoquaux G, Vaught T, Millman J, editors. *Proceedings of the 7th Python in Science Conference* Pasadena, CA USA; 2008. p. 11 – 15.

Harris CR, Millman KJ, van der Walt SJ, Gommers R, Virtanen P, Cournapeau D, Wieser E, Taylor J, Berg S, Smith NJ, Kern R, Picus M, Hoyer S, van Kerkwijk MH, Brett M, Haldane A, Fernández del Río J, Wiebe M, Peterson P, Gérard-Marchant P, et al. Array programming with NumPy. Nature. 2020; 585:357–362. doi: 10.1038/s41586-020-2649-2.

Hass J, Hertäg L, Durstewitz D. A detailed data-driven network model of prefrontal cortex reproduces key features of in vivo activity. PLOS Comput Biol. 2016; 12(5):e1004930. doi: 10.1371/journal.pcbi.1004930.

Hendrickson PJ, Yu GJ, Robinson BS, Song D, Berger TW. Towards a large-scale biologically realistic model of the hippocampus. In: *2012 Annual International Conference of the IEEE Engineering in Medicine and Biology Society* IEEE; 2012. p. 4595–4598. https://doi.org/10.1109/embc.2012.6346990, doi: 10.1109/embc.2012.6346990.

Herculano-Houzel S. The human brain in numbers: a linearly scaled-up primate brain. Front Hum Neurosci. 2009; 3:31. https://doi.org/10.3389/neuro.09.031.2009, doi: 10.3389/neuro.09.031.2009.

Herculano-Houzel S, Mota B, Wong P, Kaas JH. Connectivity-driven white matter scaling and folding in primate cerebral cortex. Proc Natl Acad Sci USA. 2010; 107(44):19008–19013. doi: 10.1073/pnas.1012590107.

Hilgetag CC, Beul SF, van Albada SJ, Goulas A. An Architectonic Type Principle Integrates Macroscopic Cortico-Cortical Connections with Intrinsic Cortical Circuits of the Primate Brain. Netw Neurosci. 2019; 3(4):905–923. doi: 10.1162/netn_a_00100.

Hodge RD, Bakken TE, Miller JA, Smith KA, Barkan ER, Graybuck LT, Close JL, Long B, Johansen N, Penn O, Yao Z, Eggermont J, Höllt T, Levi BP, Shehata SI, Aevermann B, Beller A, Bertagnolli D, Brouner K, Casper T, et al. Conserved cell types with divergent features in human versus mouse cortex. Nature. 2019; 573(7772):61–68. doi: 10.1038/s41586-019-1506-7.

Honey CJ, Thesen T, Donner TH, Silbert LJ, Carlson CE, Devinsky O, Doyle WK, Rubin N, Heeger DJ, Hasson U. Slow Cortical Dynamics and the Accumulation of Information over Long Timescales. Neuron. 2012; 76(2):423–434.

Horvát S, Gămănuț R, Ercsey-Ravasz M, Magrou L, Gămănuț B, Van Essen DC, Burkhalter A, Knoblauch K, Toroczkai Z, Kennedy H. Spatial Embedding and Wiring Cost Constrain the Functional Layout of the Cortical Network of Rodents and Primates. PLOS Biol. 2016 07; 14(7):1–30. https://doi.org/10.1371/journal.pbio.1002512, doi: 10.1371/journal.pbio.1002512.

Houweling A, Brecht M. Behavioural report of single neuron stimulation in somatosensory cortex. Nature. 2008; 451(7174):65–68. doi: 10.1038/nature06447.

Hunter JD. Matplotlib: A 2D Graphics Environment. Comput Sci Eng. 2007; 9(3):90–95. doi: 10.1109/MCSE.2007.55.

Izhikevich EM, Edelman GM. Large-scale model of mammalian thalamocortical systems. Proc Natl Acad Sci USA. 2008; 105(9):3593–3598. https://doi.org/10.1073/pnas.0712231105, doi: 10.1073/pnas.0712231105.

Johnson RR, Burkhalter A. Microcircuitry of Forward and Feedback Connections Within Rat Visual Cortex. J Comp Neurol. 1996; 368:383–398. doi: 10.1002/(SICI)1096-9861(19960506)368:3<383::AID-CNE5>3.0.CO;2-1.

Jordan J, Ippen T, Helias M, Kitayama I, Sato M, Igarashi J, Diesmann M, Kunkel S. Extremely Scalable Spiking Neuronal Network Simulation Code: From Laptops to Exascale Computers. Front Neuroinform. 2018 Feb; 12:2. https://doi.org/10.3389/fninf.2018.00002, doi: 10.3389/fninf.2018.00002.

Joseph A, Turrigiano GG. All for one but not one for all: excitatory synaptic scaling and intrinsic excitability are coregulated by CaMKIV, whereas inhibitory synaptic scaling is under independent control. J Neurosci. 2017; 37(28):6778–6785.

Kabbara A, EL Falou W, Khalil M, Wendling F, Hassan M. The dynamic functional core network of the human brain at rest. Sci Rep. 2017 Jun; 7(1):2936. doi: 10.1038/s41598-017-03420-6.

Köster J, Rahmann S. Snakemake—a scalable bioinformatics workflow engine. Biochemistry. 2012; 28(19):2520–2522. doi: 10.1093/bioinformatics/bts480.

Lamme VAF, Roelfsema PR. The distinct modes of vision offered by feedforward and recurrent processing. Trends Neurosci. 2000; 23:571–579. doi: 10.1016/S0166-2236(00)01657-X.

Layer M, Senk J, Essink S, van Meegen A, Bos H, Helias M. NNMT: Mean-Field Based Analysis Tools for Neuronal Network Models. Front Neuroinform. 2022; 16:835657. doi: 10.3389/fninf.2022.835657.

London M, Roth A, Beeren L, Häusser M, Latham PE. Sensitivity to perturbations in vivo implies high noise and suggests rate coding in cortex. Nature. 2010 July; 466(1):123–128. doi: 10.1038/nature09086.

Lu W, Zheng Q, Xu N, Feng J, Consortium D. The human digital twin brain in the resting state and in action. ArXiv. 2022; https://arxiv.org/abs/2211.15963, doi: 10.48550/ARXIV.2211.15963.

Markov NT, Ercsey-Ravasz MM, Ribeiro Gomes AR, Lamy C, Magrou L, Vezoli J, Misery P, Falchier A, Quilodran R, Gariel MA, Sallet J, Gamanut R, Huissoud C, Clavagnier S, Giroud P, Sappey-Marinier D, Barone P, Dehay C, Toroczkai Z, Knoblauch K, et al. A Weighted and Directed Interareal Connectivity Matrix for Macaque Cerebral Cortex. Cereb Cortex. 2014; 24(1):17–36. doi: 10.1093/cercor/bhs270.

Markov NT, Misery P, Falchier A, Lamy C, Vezoli J, Quilodran R, Gariel MA, Giroud P, Ercsey-Ravasz M, Pilaz LJ, Huissoud C, Barone P, Dehay C, Toroczkai Z, Van Essen DC, Kennedy H, Knoblauch K. Weight Consistency Specifies Regularities of Macaque Cortical Networks. Cereb Cortex. 2011; 21(6):1254–1272. doi: 10.1093/cercor/bhq201.

Markov NT, Vezoli J, Chameau P, Falchier A, Quilodran R, Huissoud C, Lamy C, Misery P, Giroud P, Ullman S, Barone P, Dehay C, Knoblauch K, Kennedy H. Anatomy of hierarchy: Feedforward and feedback pathways in macaque visual cortex. J Comp Neurol. 2014; 522(1):225–259. doi: 10.1002/cne.23458.

Markram H, Muller E, Ramaswamy S, Reimann MW, Abdellah M, Sanchez CA, Ailamaki A, Alonso-Nanclares L, Antille N, Arsever S, Kahou GAA, Berger TK, Bilgili A, Buncic N, Chalimourda A, Chindemi G, Courcol JD, Delalondre F, Delattre V, Druckmann S, et al. Reconstruction and simulation of neocortical microcircuitry. Cell. 2015 Oct; 163(2):456–492. https://doi.org/10.1016/j.cell.2015.09.029, doi: 10.1016/j.cell.2015.09.029.

Marques JP, Kober T, Krueger G, van der Zwaag W, Van de Moortele PF, Gruetter R. MP2RAGE, a self bias-field corrected sequence for improved segmentation and T1-mapping at high field. Neuroimage. 2010; 49(2):1271–1281. https://www.sciencedirect.com/science/article/pii/S1053811909010738, doi: 10.1016/j.neuroimage.2009.10.002.

Massimini M, Huber R, Ferrarelli F, Hill S, Tononi G. The sleep slow oscillation as a traveling wave. J Neurosci. 2004; 24(31):6862–6870.

Wes McKinney. Data Structures for Statistical Computing in Python. In: Stéfan van der Walt, Jarrod Millman, editors. *Proceedings of the 9th Python in Science Conference*; 2010. p. 56 – 61. doi: 10.25080/Majora-92bf1922-00a.

Migliore M, Cavarretta F, Hines ML, Shepherd GM. Distributed organization of a brain microcircuit analyzed by three-dimensional modeling: the olfactory bulb. Front Comput Neurosci. 2014; 8(50):1–14. doi: 10.3389/fncom.2014.00050.

Migliore M, Cavarretta F, Marasco A, Tulumello E, Hines ML, Shepherd GM. Synaptic clusters function as odor operators in the olfactory bulb. Proc Natl Acad Sci USA. 2015 Jun; 112(27):8499–8504. https://doi.org/10.1073/pnas.1502513112, doi: 10.1073/pnas.1502513112.

Minxha J, Adolphs R, Fusi S, Mamelak AN, Rutishauser U. Flexible recruitment of memory-based choice representations by the human medial frontal cortex. Science. 2020; 368(6498):eaba3313. doi: 10.1126/science.aba3313.

Moeller S, Yacoub E, Olman CA, Auerbach E, Strupp J, Harel N, Uğurbil K. Multiband multislice GE-EPI at 7 tesla, with 16-fold acceleration using partial parallel imaging with application to high spatial and temporal whole-brain fMRI. Magn Reson Med. 2010; 63(5):1144–1153. https://onlinelibrary.wiley.com/doi/abs/10.1002/mrm.22361, doi: 10.1002/mrm.22361.

Mohan H, Verhoog MB, Doreswamy KK, Eyal G, Aardse R, Lodder BN, Goriounova NA, Asamoah B, B Brakspear AC, Groot C, van der Sluis S, Testa-Silva G, Obermayer J, Boudewijns ZS, Narayanan RT, Baayen JC, Segev I, Mansvelder HD, de Kock CP. Dendritic and axonal architecture of individual pyramidal neurons across layers of adult human neocortex. Cereb Cortex. 2015; 25(12):4839–4853. doi: 10.1093/cercor/bhv188.

Monteforte M, Wolf F. Dynamical entropy production in spiking neuron networks in the balanced state. Phys Rev Lett. 2010; 105(26):268104. https://doi.org/10.1103/PhysRevLett.105.268104, doi: 10.1103/PhysRevLett.105.268104.

Nir Y, Staba RJ, Andrillon T, Vyazovskiy VV, Cirelli C, Fried I, Tononi G. Regional slow waves and spindles in human sleep. Neuron. 2011; 70(1):153–169.

Nordlie E, Gewaltig MO, Plesser HE. Towards Reproducible Descriptions of Neuronal Network Models. PLOS Comput Biol. 2009 Aug; 5(8):e1000456. https://doi.org/10.1371/journal.pcbi.1000456, doi: 10.1371/journal.pcbi.1000456.

Packer AM, Yuste R. Dense, Unspecific Connectivity of Neocortical Parvalbumin-Positive Interneurons: A Canonical Microcircuit for Inhibition? J Neurosci. 2011 Sep; 31(37):13260–13271. https://doi.org/10.1523/jneurosci.3131-11.2011, doi: 10.1523/JNEUROSCI.3131-11.2011.

Patel AX, Bullmore ET. A wavelet-based estimator of the degrees of freedom in denoised fMRI time series for probabilistic testing of functional connectivity and brain graphs. Neuroimage. 2016; 142:14–26. https://www.sciencedirect.com/science/article/pii/S1053811915003523, doi: 10.1016/j.neuroimage.2015.04.052.

Perin R, Berger TK, Markram H. A synaptic organizing principle for cortical neuronal groups. Proc Natl Acad Sci USA. 2011 Mar; 108(13):5419–5424. https://doi.org/10.1073/pnas.1016051108, doi: 10.1073/pnas.1016051108.

Potjans TC, Diesmann M. The Cell-Type Specific Cortical Microcircuit: Relating Structure and Activity in a Full-Scale Spiking Network Model. Cereb Cortex. 2014 Mar; 24(3):785–806. https://doi.org/10.1093/cercor/bhs358, doi: 10.1093/cercor/bhs358.

Priesemann V, Wibral M, Valderrama M, Pröpper R, Le Van Quyen M, Geisel T, Triesch J, Nikolic D, Munk MHJ. Spike avalanches in vivo suggest a driven, slightly subcritical brain state. Front Syst Neurosci. 2014; 8(108):80–96. http://www.frontiersin.org/systems_neuroscience/10.3389/fnsys.2014.00108/abstract, doi: 10.3389/fnsys.2014.00108.

Pronold J, Jordan J, Wylie BJN, Kitayama I, Diesmann M, Kunkel S. Routing brain traffic through the von Neumann bottleneck: Efficient cache usage in spiking neural network simulation code on general purpose computers. Parallel Comput. 2022; 113:102952. https://www.sciencedirect.com/science/article/pii/S0167819122000461, doi: 10.1016/j.parco.2022.102952.

Pronold J, Jordan J, Wylie BJN, Kitayama I, Diesmann M, Kunkel S. Routing Brain Traffic Through the Von Neumann Bottleneck: Parallel Sorting and Refactoring. Front Neuroinform. 2022; 15:785068. https://www.frontiersin.org/article/10.3389/fninf.2021.785068, doi: 10.3389/fninf.2021.785068.

Pulvermüller F, Tomasello R, Henningsen-Schomers MR, Wennekers T. Biological constraints on neural network models of cognitive function. Nat Rev Neurosci. 2021; 22:488–502. doi: 10.1038/s41583-021-00473-5.

Python Software Foundation, The Python programming language; 2008. Http://www.python.org.

Reimann MW, Anastassiou CA, Perin R, Hill SL, Markram H, Koch C. A biophysically detailed model of neocortical local field potentials predicts the critical role of active membrane currents. Neuron. 2013 Jul; 79(2):375–390. https://doi.org/10.1016/j.neuron.2013.05.023, doi: 10.1016/j.neuron.2013.05.023.

Rockland KS. What do we know about laminar connectivity? Neuroimage. 2019; 197:772–784. doi: 10.1016/j.neuroimage.2017.07.032.

Salin PA, Prince DA. Spontaneous GABAA receptor-mediated inhibitory currents in adult rat somatosensory cortex. J Neurophysiol. 1996; 75(4):1573–1588.

Schmidt M, Bakker R, Hilgetag CC, Diesmann M, van Albada SJ. Multi-scale account of the network structure of macaque visual cortex. Brain Struct Funct. 2018 Apr; 223(3):1409–1435. https://doi.org/10.1007/s00429-017-1554-4, doi: 10.1007/s00429-017-1554-4.

Schmidt M, Bakker R, Shen K, Bezgin G, Diesmann M, van Albada SJ. A multi-scale layer-resolved spiking network model of resting-state dynamics in macaque visual cortical areas. PLOS Comput Biol. 2018; 14(10):e1006359. https://doi.org/10.1371/journal.pcbi.1006359, doi: 10.1371/journal.pcbi.1006359.

Schuecker J, Schmidt M, van Albada SJ, Diesmann M, Helias M. Fundamental Activity Constraints Lead to Specific Interpretations of the Connectome. PLOS Comput Biol. 2017 Feb; 13(2):e1005179. https://doi.org/10.1371/journal.pcbi.1005179, doi: 10.1371/journal.pcbi.1005179.

Sejnowski TJ, Churchland PS, Movshon JA. Putting big data to good use in neuroscience. Nat Neurosci. 2014 Nov; 17(11):1440–1441. https://doi.org/10.1038/nn.3839, doi: 10.1038/nn.3839.

Senk J, Kriener B, Djurfeldt M, Voges N, Jiang HJ, Schüttler L, Gramelsberger G, Diesmann M, Plesser HE, van Albada SJ. Connectivity Concepts in Neuronal Network Modeling. PLOS Comput Biol. 2022; 18(9):e1010086. doi: 10.1371/journal.pcbi.1010086.

Shapson-Coe A, Januszewski M, Berger DR, Pope A, Wu Y, Blakely T, Schalek RL, Li PH, Wang S, Maitin-Shepard J, Karlupia N, Dorkenwald S, Sjostedt E, Leavitt L, Lee D, Bailey L, Fitzmaurice A, Kar R, Field B, Wu H, et al. A connectomic study of a petascale fragment of human cerebral cortex. BioRxiv. 2021; doi: 10.1101/2021.05.29.446289.

Sheroziya M, Timofeev I. Global intracellular slow-wave dynamics of the thalamocortical system. J Neurosci. 2014; 34(26):8875–8893.

Sherwood CC, Miller SB, Karl M, Stimpson CD, Phillips KA, Jacobs B, Hof PR, Raghanti MA, Smaers JB. Invariant synapse density and neuronal connectivity scaling in primate neocortical evolution. Cereb Cortex. 2020; 30(10):5604–5615. doi: 10.1093/cercor/bhaa149.

Shinomoto S, Kim H, Shimokawa T, Matsuno N, Funahashi S, Shima K, Fujita I, Tamura H, Doi T, Kawano K, Inaba N, Fukushima K, Kurkin S, Kurata K, Taira M, Tsutsui KI, Komatsu H, Ogawa T, Koida K, Tanji J, et al. Relating Neuronal Firing Patterns to Functional Differentiation of Cerebral Cortex. PLOS Comput Biol. 2009; 5(7):e1000433. doi: 10.1371/journal.pcbi.1000433.

Smith SM, Jenkinson M, Woolrich MW, Beckmann CF, Behrens TEJ, Johansen-Berg H, Bannister PR, De Luca M, Drobnjak I, Flitney DE, Niazy RK, Saunders J, Vickers J, Zhang Y, De Stefano N, Brady JM, Matthews PM. Advances in functional and structural MR image analysis and implementation as FSL. Neuroimage. 2004; 23:S208–S219. https://www.sciencedirect.com/science/article/pii/S1053811904003933, doi: 10.1016/j.neuroimage.2004.07.051, mathematics in Brain Imaging.

Spruston N, Jonas P, Sakmann B. Dendritic glutamate receptor channels in rat hippocampal CA3 and CA1 pyramidal neurons. J Physiol. 1995; 482(2):325–352.

Squire LR, Genzel L, Wixted JT, Morris RG. Memory consolidation. Cold Spring Harbor Perspectives in Biology. 2015; 7(8):a021766.

Stephan KE, Kamper L, Bozkurt A, Burns GAPC, Young MP, Kötter R. Advanced database methodology for the collation of connectivity data on the macaque brain (CoCoMac). Philos Trans R Soc B. 2001; 356:1159–1186. doi: 10.1098/rstb.2001.0908.

Teeter C, Iyer R, Menon V, Gouwens N, Feng D, Berg J, Szafer A, Cain N, Zeng H, Hawrylycz M, Koch C, Mihalas S. Generalized leaky integrate-and-fire models classify multiple neuron types. Nat Commun. 2018; 9:709. doi: 10.1038/s41467-017-02717-4.

Theodoni P, Majka P, Reser DH, Wójcik DK, Rosa MGP, Wang XJ. Structural Attributes and Principles of the Neocortical Connectome in the Marmoset Monkey. Cereb Cortex. 2021 07; 32(1):15–28. doi: 10.1093/cercor/bhab191.

Van Essen DC, Smith SM, Barch DM, Behrens TE, Yacoub E, Ugurbil K, Consortium WMH, et al. The WU-Minn Human Connectome Project: An overview. Neuroimage. 2013; 80:62–79. doi: 10.1016/j.neuroimage.2013.05.041.

Vandevelde I, Duckworth E, Reep R. Layer VII and the gray matter trajectories of corticocortical axons in rats. Anatomy and Embryology. 1996; 194:581–593.

Virtanen P, Gommers R, Oliphant TE, Haberland M, Reddy T, Cournapeau D, Burovski E, Peterson P, Weckesser W, Bright J, van der Walt SJ, Brett M, Wilson J, Millman KJ, Mayorov N, Nelson ARJ, Jones E, Kern R, Larson E, Carey CJ, et al. SciPy 1.0: Fundamental Algorithms for Scientific Computing in Python. Nat Methods. 2020; 17:261–272. doi: 10.1038/s41592-019-0686-2.

Von Economo C. Cellular Structure of the Human Cerebral Cortex. Karger Medical and Scientific Publishers; 2009. Translated and edited by L.C. Triarhou.

Wagstyl K, Larocque S, Cucurull G, Lepage C, Cohen JP, Bludau S, Palomero-Gallagher N, Lewis LB, Funck T, Spitzer H, et al. BigBrain 3D atlas of cortical layers: Cortical and laminar thickness gradients diverge in sensory and motor cortices. PLOS Biol. 2020; 18(4):e3000678.

Waskom ML. seaborn: statistical data visualization. Journal of Open Source Software. 2021; 6(60):3021. https://doi.org/10.21105/joss.03021, doi: 10.21105/joss.03021.

Watts DJ, Strogatz SH. Collective dynamics of small-world networks. Nature. 1998; 393:440–442. doi: 10.1038/30918.

Winnubst J, Bas E, Ferreira TA, Wu Z, Economo MN, Edson P, Arthur BJ, Bruns C, Rokicki K, Schauder D, et al. Reconstruction of 1,000 projection neurons reveals new cell types and organization of long-range connectivity in the mouse brain. Cell. 2019; 179(1):268–281. doi: 10.1016/j.cell.2019.07.042.

Yamaura H, Igarashi J, Yamazaki T. Simulation of a Human-Scale Cerebellar Network Model on the K Computer. Front Neuroinform. 2020; 14:16. https://www.frontiersin.org/articles/10.3389/fninf.2020.00016, doi: 10.3389/fninf.2020.00016.

Zachlod D, Palomero-Gallagher N, Dickscheid T, Amunts K. Mapping cyto-and receptor architectonics to understand brain function and connectivity. Biological Psychiatry. 2023; 93(5):471–479.

Appendix

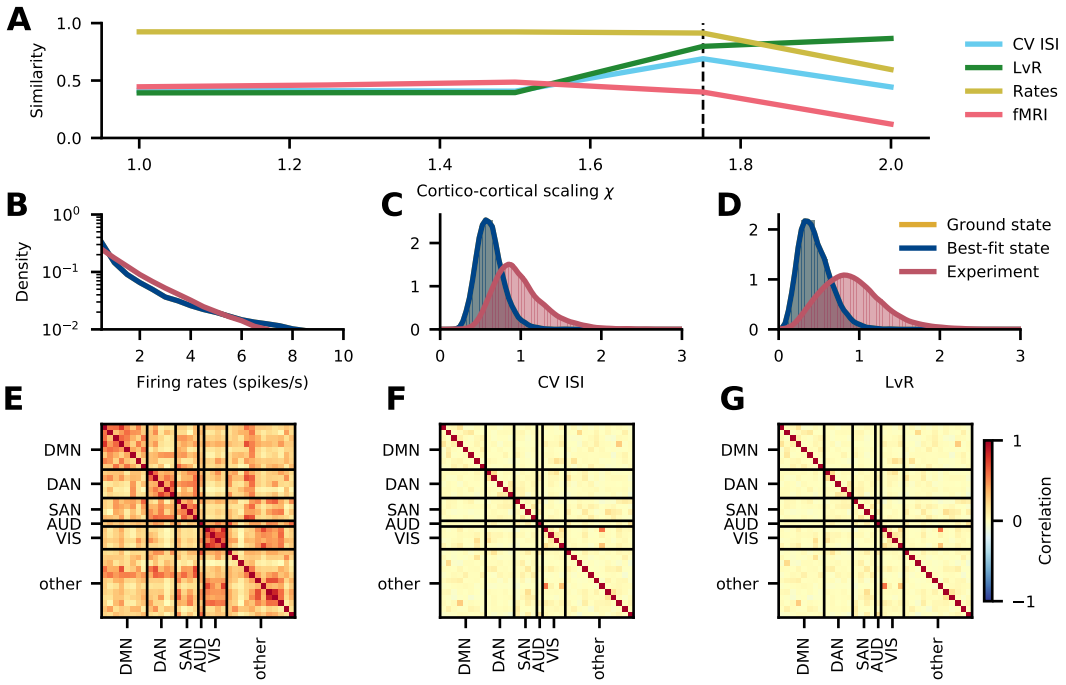

Figure 9. Scaling plot with $g = -2$. Simulations abruptly fail at $\chi > 2$ and reach a high-activity state that cannot be simulated in a reasonable time. The vertical dashed line at $\chi = 1.75$ corresponds to the chosen best-fit state where the agreement with experimental data is maximized. The similarities of the CV ISI, LvR, and rates stay flat across all simulated χ while the fMRI similarity slightly increases **(A)**. The firing rate **(B)**, CV ISI **(C)**, and LvR **(D)** distributions of the ground and best-fit states do not differ significantly and, while the rate distributions are close to the experimental data, the irregularity distributions are not. The functional connectivities of the ground state **(F)** and best-fit state **(G)** are weak, unlike the experimental functional connectivity **(E)**.

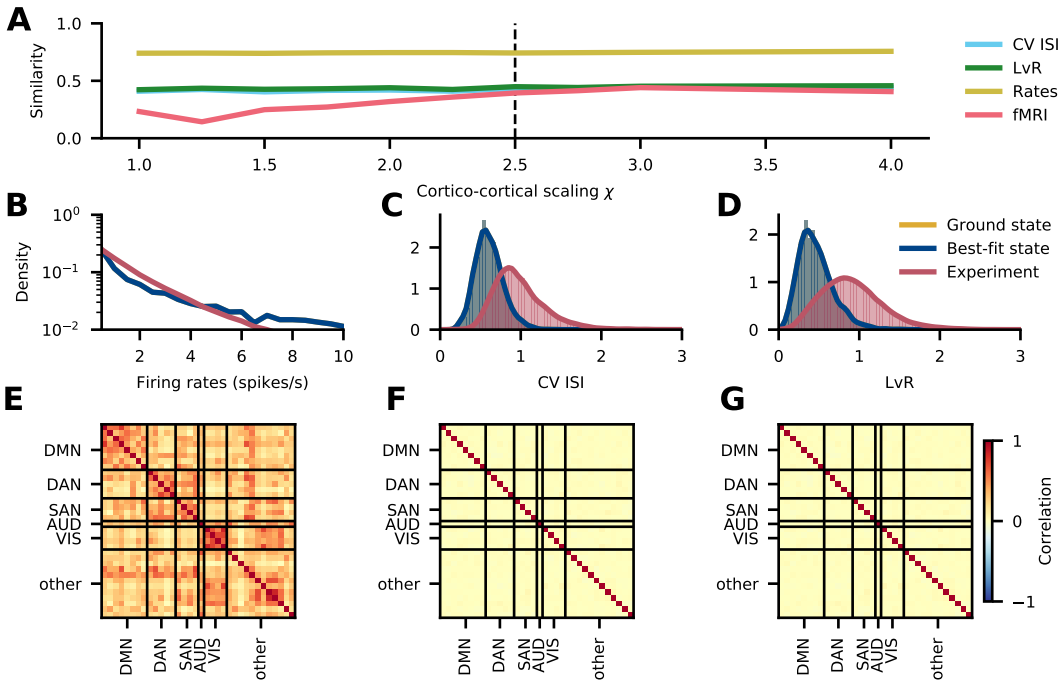

Figure 10. Scaling plot with neuron parameters distributed according to the values for human neurons from the Allen Cell Types Database (https://celltypes.brain-map.org/; cf. Further Parameters of the Model). As this realization of the model does not show a unique best-fit state, the vertical line at $\chi = 2.5$ shows the chosen best-fit state, similar to the original model. While the functional connectivity benefits from increasing the cortico-cortical scaling factors , all other similarities stay constant. Simulations at $\chi > 4$ reach a high-activity state that cannot be simulated in a reasonable time. **(A)**. The rates are explained equally well in the ground state and best-fit state, but less well than in the model without distributed neuron parameters (cf. Fig. 5) **(B)**. The CV ISI is not well explained in the ground nor in the best-fit state **(C)**. The LvR in the best-fit state, in contrast to the ground state, matches the experimental data reasonably well **(D)**. The functional connectivity in both the ground state **(F)** and the best-fit state **(G)** is weak, unlike the experimental functional connectivity **(E)**, although the similarity measure indicates that the best-fit state captures the structure of the functional connectivity better.

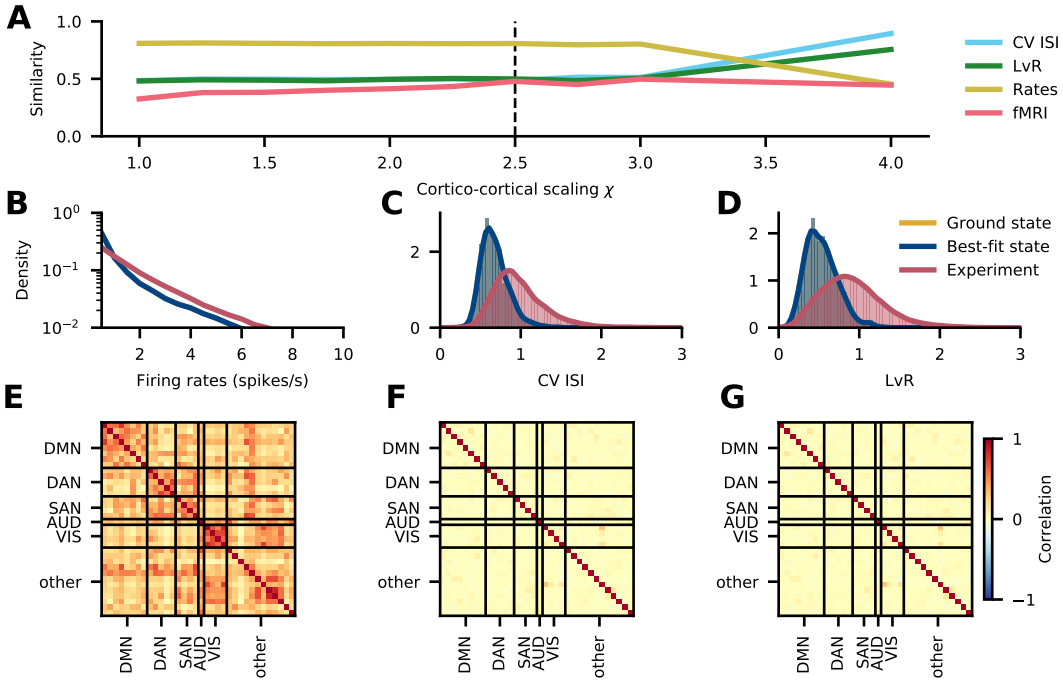

Figure 11. Scaling plot with different synaptic time constants, $\tau_{s,E} = 2$ and $\tau_{s,I} = 4$. As this realization of the model does not show a unique best-fit state, the vertical line at $\chi = 2.5$ shows the chosen best-fit state, similar to the original model. While the LvR and CV ISI benefit from cortico-cortical scaling factors , the similarity between the simulated and experimental rate distributions degrades and the similarity of the functional connectivity stays constant. **(A)**. The rates are better explained in the ground state **(B)**, whereas the CV ISI **(C)** and LvR **(D)** distributions are nearly the same in both states, and do not match the experimental data. The functional connectivity in both the ground state **(F)** and the best-fit state **(G)** is weak. Neither matches the experimental functional connectivity **(E)** in size, although the similarity measure shows that the structure is fairly well captured.

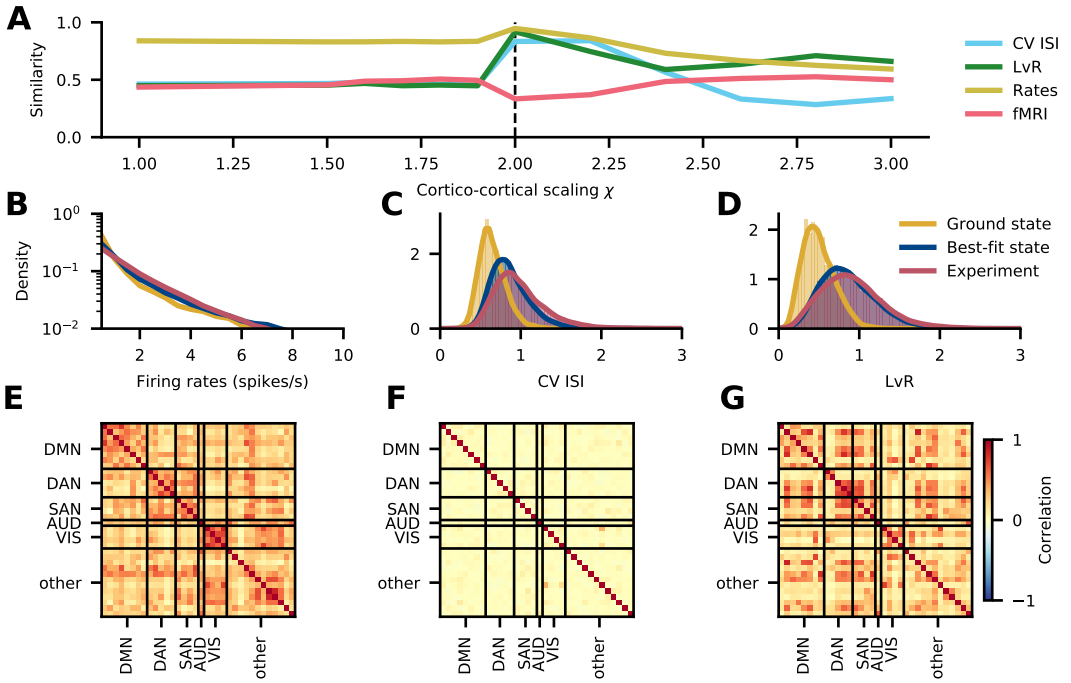

Figure 12. Scaling plot using layer-resolved excitatory-to-inhibitory ratios of neuron densities from ***Binzegger et al.*** (***2004***); ***Potjans and Diesmann*** (***2014***). The main difference compared to ***Shapson-Coe et al.*** (***2021***) is the higher fraction of excitatory cells in layer 2/3: 0.78 vs. 0.65. The other fractions are similar between the two studies: layer 4: 0.80 vs. 0.79, layer 5: 0.82 vs. 0.78, and layer 6: 0.83 vs. 0.86 for ***Binzegger et al.*** (***2004***); ***Potjans and Diesmann*** (***2014***) and ***Shapson-Coe et al.*** (***2021***), respectively. In this model realization, the additional scaling parameter χ_I for cortico-cortical connections onto inhibitory neurons is $\chi_I = 1$. The similarities of rates, CV ISI, LvR, and functional connectivity stay roughly constant for cortico-cortical scaling factors $\chi < 2$. The best-fit state is shown as a dashed vertical line at $\chi = 2$. Here, the distributions of rates, CV ISI, and LvR almost perfectly match the experimental data, while the similarity of the functional connectivity is slightly worse than in the ground state. For $\chi > 2$, the similarities of rates, CV ISI, and LvR slowly deteriorate, while the functional connectivity similarity improves **(A)**. The firing rates match the experimental data well in both states **(B)**, and the CV ISI **(C)** and LvR **(D)** in the best-fit state closely agree with the experimental data. The functional connectivity in the ground state is uniformly weak **(F)**, while it is more differentiated in the best-fit state **(G)**. Interestingly, the pattern of functional connectivity of the ground state matches the experimental functional connectivity **(E)** better than that of the state with the best overall fit**.**

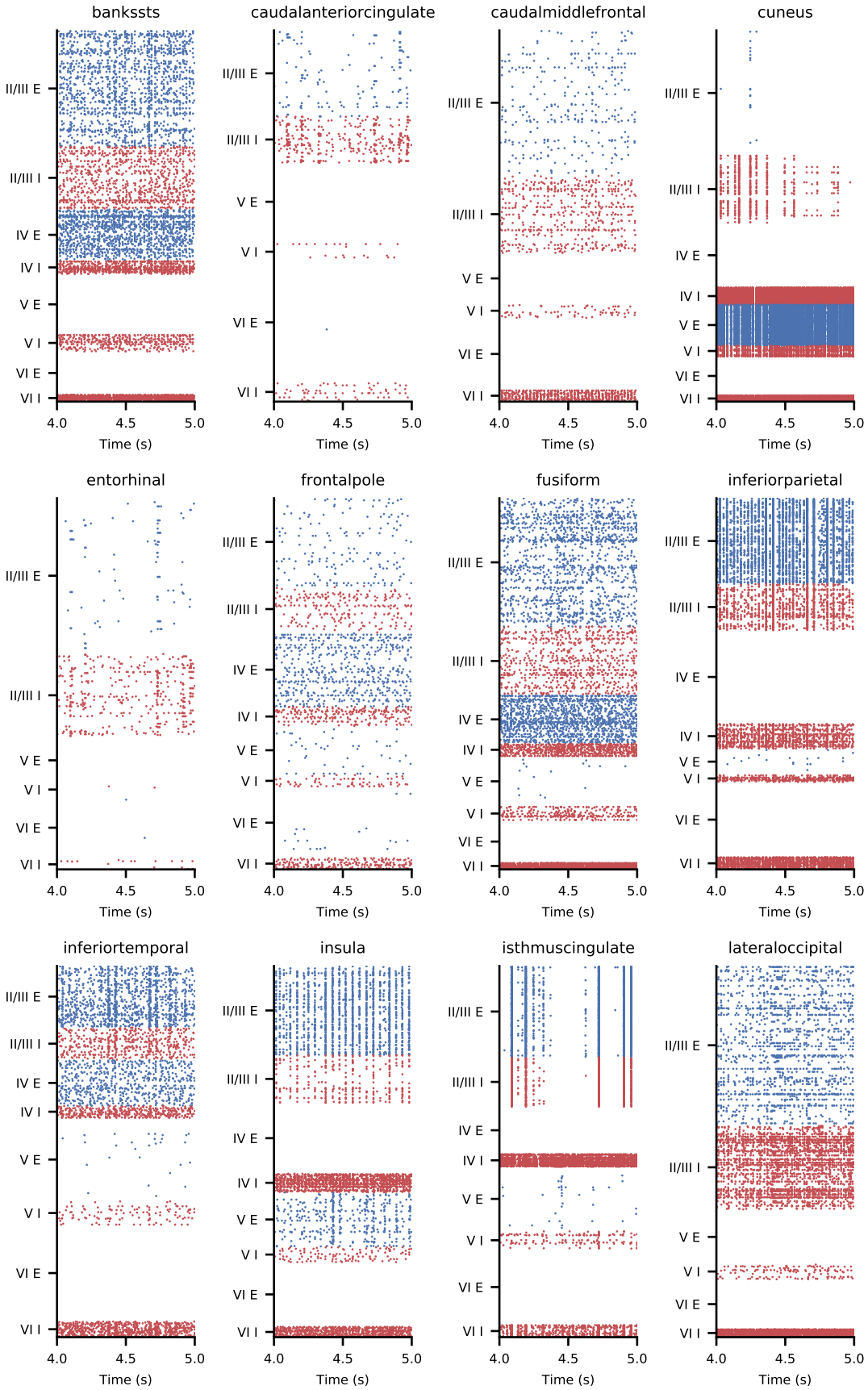

Figure 13. Raster plots in the best-fit state. Subsampled to 2.5% of the excitatory (blue) and inhibitory (red) neurons.

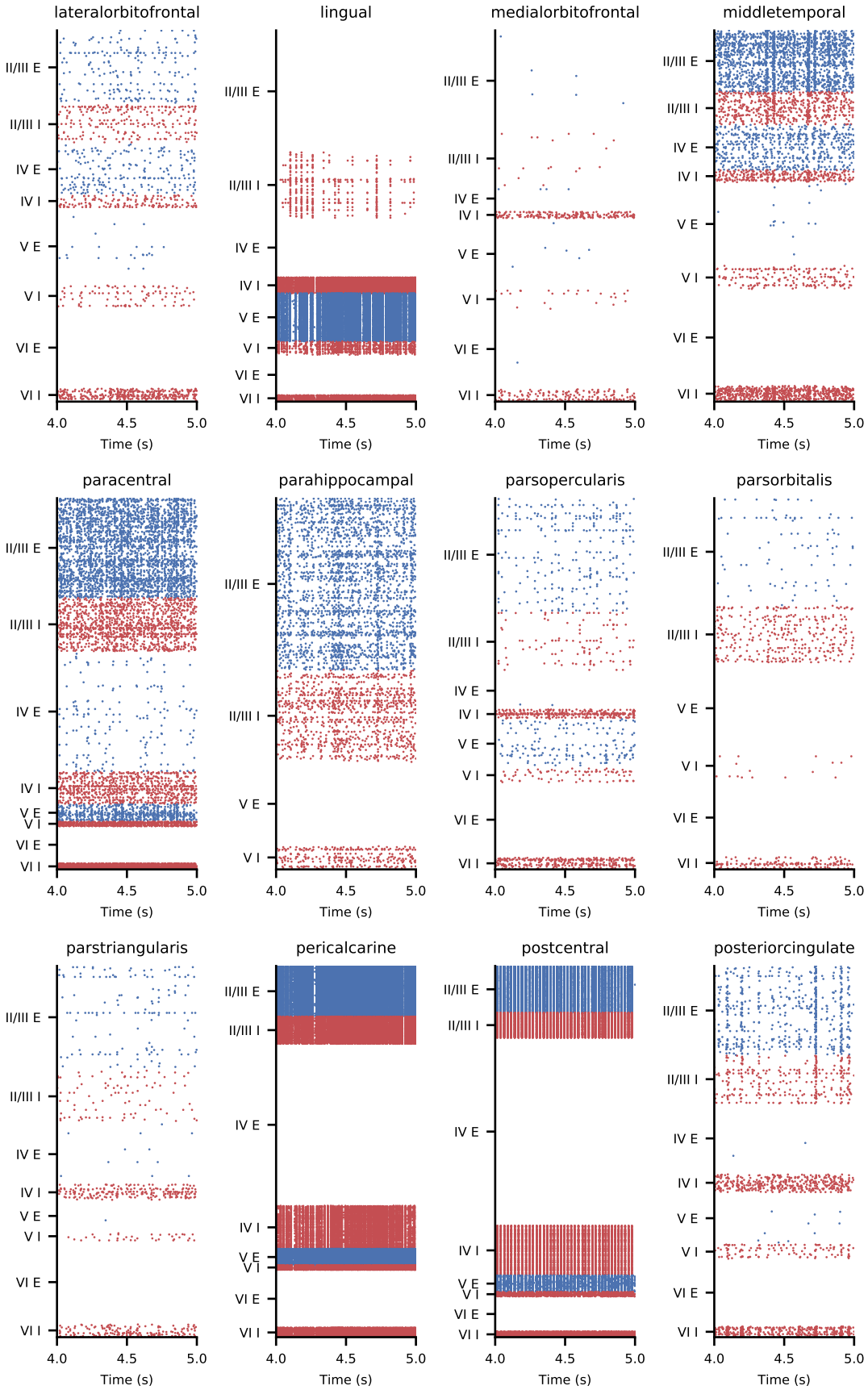

Figure 14. Raster plots in the best-fit state. Subsampled to 2.5% of the excitatory (blue) and inhibitory (red) neurons.

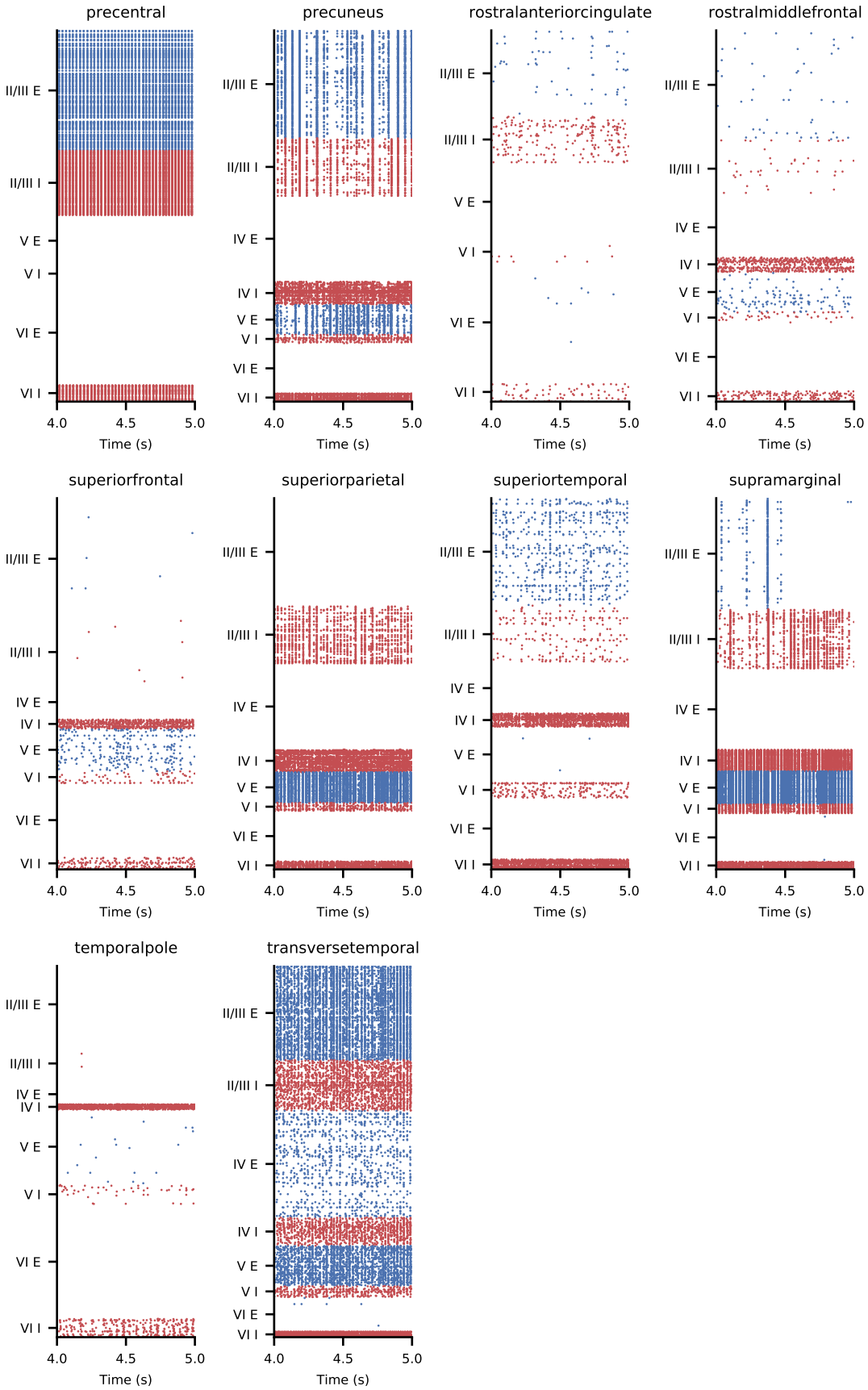

Figure 15. Raster plots in the best-fit state. Subsampled to 2.5% of the excitatory (blue) and inhibitory (red) neurons.